possibility of noninvasive imaging of the course and healing of small-intestine ulceration. In the present study, we noninvasively observed a newly created small-intestine ulceration and its healing using ^{18}F-FDG PET. We used macro- and microautoradiographic studies, combined with immunohistochemistry, to identify the origin of the ^{18}F-FDG signals, also revealing a transition in signal between the occurrence and healing of the ulcer.

MATERIALS AND METHODS

Animals

Male Sprague–Dawley rats (Nippon Charles River; age, 8 wk) were used in all experiments. The rats were housed in a cage with a raised mesh base, under constant environmental conditions (room temperature, 22°C−24°C; relative humidity, 60%−70%) and a 12 h−12 h light–dark cycle. Food and water were provided ad libitum. The experimental procedures used in the present study were approved by the Animal Care Committee of the Osaka City University Graduate School of Medicine. All efforts were made to minimize animal suffering and the number of animals used for the studies.

Induction of Small-Intestine Ulceration and Determination of Myeloperoxidase Activity

Small-intestine ulceration was induced by subcutaneous administration of indomethacin (Sigma-Aldrich) suspended in saline with a drop of polysorbate 80 (ICN Biomedicals Inc.) at a dose of 10 mg/kg. At 1, 2, 4, and 7 d after indomethacin administration, the rats were euthanized under deep ether anesthesia. To visualize the intestinal lesions, 1 mL of Evans blue dye (Wako Pure Chemical Industries Ltd.; 1% w/v) was injected intravenously 30 min before euthanasia in 2–3 indomethacin-administered animals. The small intestine was removed and fixed with 2% formalin.

Myeloperoxidase activity was measured to evaluate neutrophil infiltration into the intestinal mucosa according to the method reported by Krawisz et al. (*23*), with some modification. Four to five animals were used on each experimental day (days 1, 2, 4, and 7). The animals were euthanized under deep ether anesthesia at 1, 2, 4, and 7 d after indomethacin administration. Blood was then totally withdrawn by perfusion with ice-cold saline through the left ventricle. The small intestine was removed, and the wall along the opposite side of the mesenteric attachment was cut. After the tissue was rinsed with saline, the small intestine was homogenized with a 50 mmol/L concentration of phosphate buffer containing 0.5% (w/v) hexadecyl-trimethyl-ammonium bromide (Wako). The homogenized samples were subjected to freezing and thawing 3 times and centrifuged at 2,000 rpm for 10 min at 4°C. Supernatant (100 μL) was added to 1.9 mL of 10 mmol/L phosphate buffer (pH 6.0), to which 1 mL of 1.5 mol/L *o*-dianisine dihydrochloride (Sigma-Aldrich) containing 0.0005% (w/v) hydrogen peroxide (H_2O_2) was added. Absorbance at 450 nm of each sample was assessed using a spectrophotometer (Beckman Instruments). Protein content was measured using a modified bicinchoninic acid assay method (bicinchoninic acid protein assay reagent kit; Pierce). Myeloperoxidase activity was obtained from the slope of the reaction curve, on the basis of the following equation for specific activity:

$$\mu\text{mol } H_2O_2/\text{min/mg protein} = (\text{OD/min})/\text{OD}/\mu\text{mol } H_2O_2 \times \text{mg protein}.$$

^{18}F-FDG PET

^{18}F was produced by the ^{18}O(p, n)^{18}F nuclear reaction in a cyclotron at the Osaka City University, and ^{18}F-FDG was synthesized by the method reported by Hamacher et al. (*24*) using an automated ^{18}F-FDG synthesis system (JFE Steel Co.).

We used a small-animal PET scanner (microPET Focus220; Siemens Medical Solutions Inc.) with an animal port (diameter, 220 mm; axial extent, 78 mm; parallel slices, 95; and spatial resolution, 1.7 mm in full width at half maximum at the center of the field of view). The scanner had a detector system comprising 47 crystal rings made of lutetium oxyorthosilicate; 3-dimensional list-mode data were acquired. At 7 d before treatment and at 1, 2, and 7 d after indomethacin administration, PET scans were obtained on 4 rats. ^{18}F-FDG, at an activity of 55.5 MBq/kg in 0.3 mL of saline, was administered to each rat via the tail vein while the animal was conscious. At 45 min after the ^{18}F-FDG administration, the rats were injected intravenously with propofol (Diprivan; Zeneca) at a dose of 10 mg/kg, followed by continuous infusion at 40 mg/kg/h during the PET scan, as previously reported (*25*). Emission data were then acquired for 20 min, with an energy window of 400–650 keV and a coincidence-timing window of 6 ns. The scanned area was 7.8 cm, from the stomach to the bladder, including the entire intestinal area. From 50 to 70 min after the injection of ^{18}F-FDG, emission data were sorted into a single-frame sinogram, with a span of 3 and a ring difference of 47, and reconstructed using filtered backprojection and maximum a posteriori algorithms. To clearly visualize the intestinal ulceration, maximum-intensity-projection images of the maximum a posteriori–reconstructed images were displayed using ASIPro software (version 4.10; Concorde Microsystems).

In our model of indomethacin-induced small-intestine ulcers, the diameter of each ulcer was approximately 1.0–1.5 mm (data not shown). Consequently, circular regions of interest (ROIs) (diameter, 1 mm) were drawn on the abdominal area (except the kidney, bladder, or bone) in the filtered backprojection–reconstructed images, using PMOD (version 2.75; PMOD Technologies Ltd.). A total of 7–8 ROIs were selected from the most intense signal in 7 consecutive filtered backprojection–reconstructed images from each animal. The ROI values were averaged to produce mean standardized uptake values (SUVs) based on the following equation for quantitative comparison of ^{18}F-FDG uptake. The mean SUV obtained from 50 to 60 ROIs was used as the data for each animal. These data were plotted against time (days) after indomethacin administration:

$$\text{SUV} = \text{mean ROI value (MBq/mL)}/\{\text{injected activity (MBq)/body weight (g)}\}$$

γ-Counting Study

Healthy rats and those with ulcers (1 d after indomethacin administration) were injected with ^{18}F-FDG at a dose of 55.5 MBq/kg via the tail vein. Rats (n = 4–6 animals in each group) were euthanized at 5, 15, 30, 45, and 90 min after ^{18}F-FDG injection under deep ether anesthesia. A 5-cm length of ileum was taken from the region 5–20 cm above the colon, washed with

saline, and weighed. Radioactivity of ^{18}F-FDG in each sample was counted using an auto-well γ-counting system (ARC-2000; ALOKA Co. Ltd.). In addition, we evaluated radioactivity at 45 min after ^{18}F-FDG injection among the different time intervals (1, 2, 4, and 7 d after injection of indomethacin). The amount of radioactivity in each tissue was calculated as the percentage injected dose per gram of tissue (%ID/g).

Macroautoradiography

Macroautoradiography was performed using a modified method described in our previous study, as reported by Matsumura et al. (*25*). Briefly, ^{18}F-FDG (55.5 MBq/kg) in 0.3 mL of physiologic saline was administered to rats via the tail vein. At 45 min after administration, the rats were deeply anesthetized with diethyl ether and then euthanized, and the blood was totally withdrawn by perfusing saline through the left ventricle. The small intestine was then rapidly removed, washed with saline, and placed on an imaging plate (BAS-IV MS 2040; Fuji Photo Film) for 20 min. The plate was scanned with a bioimaging analyzer (BAS-5000; Fuji Photo Film), and the images were displayed by Image Gauge software (version 4.2.1; Fuji Photo Film).

Microautoradiography Combined with Immunohistochemistry

Microautoradiography was performed using a modified method reported by Kubota et al. (*26*). Briefly, healthy rats and those with ulcers were injected intravenously with ^{18}F-FDG (74 MBq). They were euthanized under deep ether anesthesia at 45 min after the administration. Blood was totally withdrawn by perfusing saline through the left ventricle. The small intestine was quickly dissected and frozen with dry ice. Under a safety light, 5-μm-thick sections were made and mounted on slides coated with NTB2 nuclear emulsion (Kodak) diluted 13:7 with distilled water. The slides were immediately frozen on a dry ice block and kept in exposure boxes cooled with dry ice. After a 6-h exposure, sections were transferred to ethanol and acetic acid (ratio, 19:1) at −70°C and 25°C for 1 min each. After washing with water twice for 3 min, the sections were developed in D-19 developer (Kodak) for 5 min, fixed in Fuji Fix (Fuji Photo Film) for 15 min at room temperature, and then washed in water for 10 min.

In the combined microautoradiography and immunohistochemistry study, sections were fixed by 4% paraformaldehyde at 4°C for 3 min after development and fixation for microautoradiography. We inactivated the endogenous peroxidase by immersing the sections in 0.3% H_2O_2 in isotonic phosphate-buffered saline with 0.3% Triton X-100 (PBS-T) (Sigma-Aldrich) at room temperature for at least 2 h and then washing the sections with PBS-T 3 times for 5 min each. After immersing the sections in a blocking solution (3% normal serum in PBS-T) at room temperature for 1 h, we incubated the sections with each antibody at 4°C for 18 h as follows: monoclonal antibodies against rat CD31 (an endothelial cell marker; BD Biosciences Pharmingen) (1:200 dilution), rat ED2 (a macrophage marker; Serotec Ltd.) (1:100 dilution), and human α-smooth muscle actin (α-SMA, a myofibroblast marker; R&D Systems) (1:200 dilution), and a polyclonal antibody against Ki67 (a proliferation marker; Novocastra Laboratories) (1:1,000 dilution). After we washed the sections in PBS-T 3 times, we incubated them with biotinylated antimouse or antirabbit IgG (Vector Laboratories; 1:400 dilution) at room temperature for 4 h, washed them with PBS-T 3 times, and then incubated them with peroxidase-labeled streptavidin (Vectastain; Vector Laboratories) at room temperature for 1 h. These immunoreactions were visualized by the reaction with 3,3′-diaminobenzidine (Wako) and 0.03% H_2O_2. Counterstaining was performed with Mayer's hematoxylin.

Statistical Analysis

Parametric data are presented as mean ± SD. Statistical significance was determined using a 2-tailed Student *t* test. A *P* value of less than 0.05 was considered to be statistically significant.

RESULTS

Induction of Indomethacin-Induced Intestinal Ulcer and Myeloperoxidase Activity Assay

Administration of indomethacin (10 mg/kg) caused small-intestine ulceration on the side of the mesenteric attachment 24 h after administration, mainly in the ileum. Intestinal ulcers were most severe at day 1 (24 h after indomethacin administration), after which gradual healing was observed (Fig. 1A). Macroscopically, ulcers were almost healed in 7 d (Fig. 1A). Histologic observation revealed denuded epithelium and severe edema in the submucosa on day 1. Granulation tissue was clearly observed on the ulcer bed on day 4, and neoepithelial cells covered the damaged areas on day 7 (Fig. 1B). These macro- and microscopic observations are consistent with a report by Hatazawa et al. (*27*).

To evaluate the severity of ulceration by quantifying infiltration of neutrophils, myeloperoxidase activity was assayed in the small-intestine mucosa. In the control group (Fig. 1C), little myeloperoxidase activity was detected in the intestine (<0.01 μmol H_2O_2/mg protein). On day 1, myeloperoxidase activity was markedly elevated (0.38 ± 0.04 μmol H_2O_2/mg protein), a value significantly higher than that of the control group ($P < 0.01$). Myeloperoxidase activity began to decline on day 2 (0.21 ± 0.10 μmol H_2O_2/mg protein [$P < 0.05$] on day 2 and 0.04 ± 0.01 μmol H_2O_2/mg [$P < 0.05$] on day 4), and activity was negligible on day 7 (<0.01 μmol H_2O_2/mg protein).

γ-Counting Study

^{18}F-FDG accumulation in the small intestine on day 1 after indomethacin administration was evaluated by γ-counting using small intestines taken at 5, 15, 30, 45, and 90 min after ^{18}F-FDG injection (Supplemental Fig. 1; supplemental materials are available online only at http://jnm.snmjournals.org). Accumulation in the intestines with ulcers reached a maximum at 45 min after ^{18}F-FDG injection, before decreasing. In contrast, ^{18}F-FDG uptake in control animals injected with vehicle alone peaked 5 min after ^{18}F-FDG injection, before decreasing.

In the course of small-intestine ulceration and healing for the 7 d after indomethacin administration, γ-counting was performed 45 min after the injection on days 1, 2, 4, and 7 in indomethacin-treated and control (vehicle-injected) rats (Fig. 2). In indomethacin-treated rats, the highest value was observed on day 1 (1.05 ± 0.37 %ID/g, $n = 6$ animals),

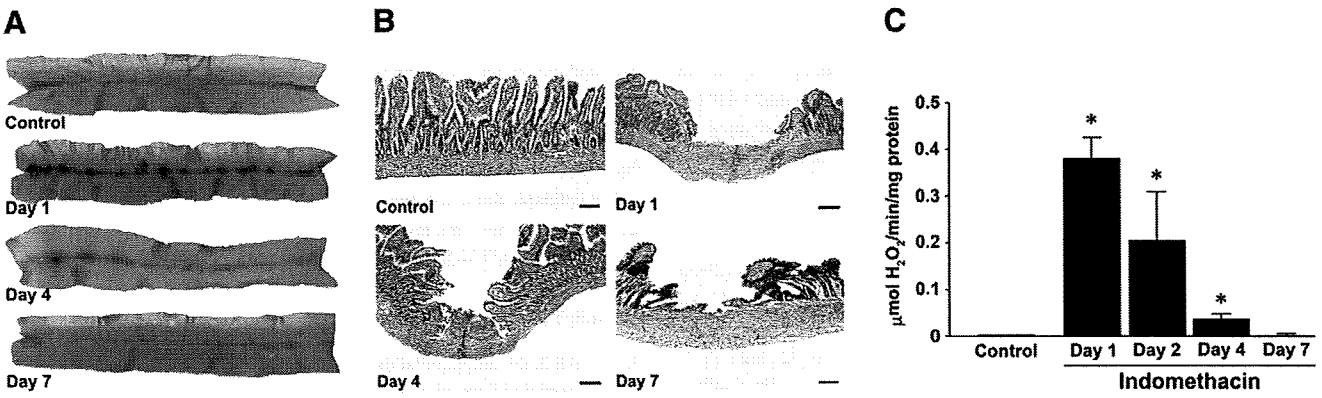

FIGURE 1. Macroscopic (A) and microscopic (B) observations of indomethacin-induced small-intestine ulceration during healing in rats. (A) Continuous circular lesions were seen on side of mesenteric attachment on day 1 or 4. (B) Histologically, denuded epithelium and severe edema in submucosa (day 1), granulation tissue on ulcer bed (day 4), and neoepithelial cells (day 7) were observed (hematoxylin and eosin staining; scale bar, 200 μm). (C) Change in myeloperoxidase activity as marker of neutrophil infiltration during indomethacin-induced intestinal ulceration and healing. Myeloperoxidase activity was evaluated in animals after administration of indomethacin (days 1, 2, 4, and 7) and in vehicle-injected animals (control). Data are shown as mean ± SD; n = 4–5 animals. *$P < 0.05$.

after which the values gradually decreased (0.78 ± 0.17 %ID/g, n = 6 animals on day 2 and 0.55 ± 0.15 %ID/g, n = 6 animals on day 4), returning to the value of 0.21 ± 0.12 %ID/g on day 7 (the same level as in the control rats [0.25 ± 0.07 %ID/g, n = 4 animals]).

Small-Animal PET Study

In the ^{18}F-FDG PET study, specific ^{18}F-FDG accumulation was visualized and quantified in coronal images of the abdominal areas of 4 rats in the course of small-intestine ulceration and healing for 7 d after indomethacin administration (Fig. 3). Over the course of the experiment, accumulations were commonly observed in the kidney and urinary bladder. On day 1, robust tubelike signals were seen in the abdominal area (Fig. 3A, arrowhead). Similar but weak signals were seen on day 2. These specific signals finally disappeared on day 7 (Fig. 3A).

Figure 3B indicates the mean SUV in the abdominal areas of the animals on each experimental day of the ^{18}F-FDG PET study. SUV was highest on day 1 (2.16 ± 0.28, $P < 0.01$), began to decrease on day 2 (1.91 ± 0.87, $P < 0.05$), and returned to the pretreatment level (0.70 ± 0.08) on day 7 (0.91 ± 0.17), consistent with the findings of the γ-counting study.

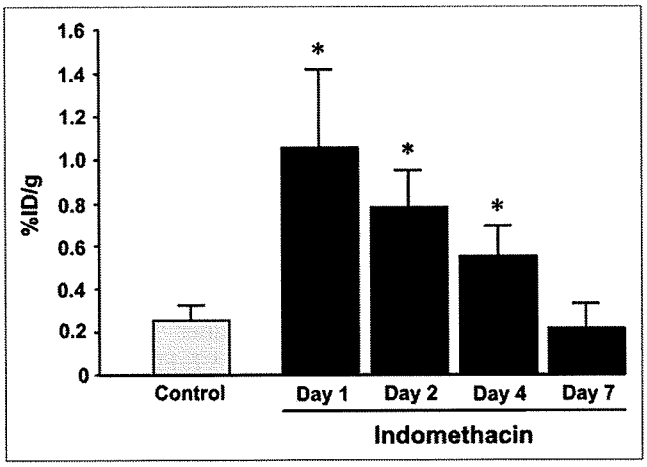

FIGURE 2. γ-counting study of ^{18}F-FDG uptake in ulcerated intestine, showing ^{18}F-FDG accumulation in small intestine at time points after indomethacin administration (days 1, 2, 4, and 7) and after vehicle injection (control). Data are shown as mean ± SD; n = 6–8 animals for each time point.

Macroautoradiography

The autoradiography findings were analyzed for ex vivo confirmation of the region of ^{18}F-FDG accumulation in the small intestine (Fig. 4). In the control group (injected with vehicle alone), low and uniform distribution of ^{18}F-FDG was observed throughout the intestine. On day 1 after indomethacin administration, discontinuous dotlike accumulation was clearly identified, mainly in the ileum. In the specimen opened along the longitudinal axis, intensive accumulation of ^{18}F-FDG was observed at the mesenteric side of the intestinal mucosa in which ulceration was observed (Fig. 4, arrowhead). On day 7, the ^{18}F-FDG imaging profile was similar to that of the control.

Microautoradiography Combined with Immunohistochemistry

Microautoradiography of the intestine was performed to identify ^{18}F-FDG accumulation at the cellular level (Figs. 5 and 6). In animals injected with indomethacin, labeling with silver grains of a high density was observed in ulcerated areas, especially in the submucosal and smooth muscle layers on day 1 (Figs. 5A–5C). Combined with peroxidase staining, silver grains were seen in the ulcerated

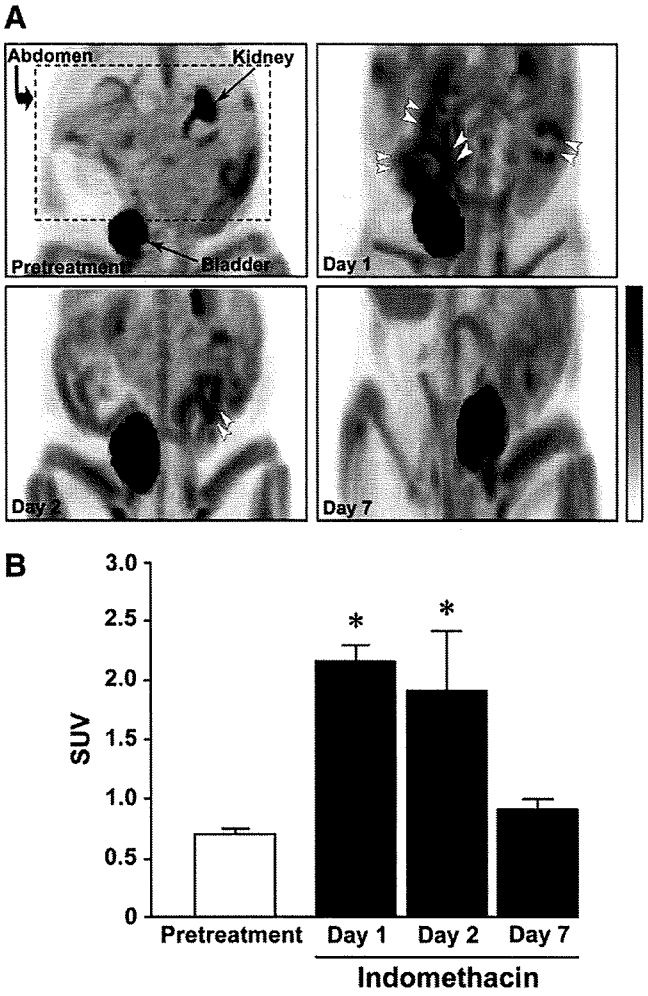

FIGURE 3. ^{18}F-FDG PET study of indomethacin-induced intestinal ulceration. (A) Abdominal PET images (coronal images) in same rat at different times after indomethacin administration. Arrowheads indicate characteristic accumulation of ^{18}F-FDG. (B) Quantification of ^{18}F-FDG uptake in PET study. Mean SUVs are shown as mean ± SD; $n = 4$ animals. *$P < 0.05$.

area that included the majority of the peroxidase-positive cells (Figs. 6A and 6B).

On day 4, dense labeling with silver grains was seen on cells forming granulation tissue (Figs. 5D and 5E). In granulation tissue, combined microautoradiography and immunohistochemistry revealed silver grains localized on the cytoplasm of α-SMA–positive myofibroblasts, a few ED2-positive macrophages, and CD31-positive endothelial cells (Figs. 6C–6E).

^{18}F-FDG accumulation was observed not only in the intestinal crypts and around ulcerated areas but also in the intact region of the intestine. The microautoradiographic study combined with immunohistochemical detection of Ki67, a cell cycle marker, revealed that such an accumulation of ^{18}F-FDG was involved in many proliferating cells in the crypts (Fig. 6F).

DISCUSSION

In recent years, the usability of ^{18}F-FDG PET has been reported for the detection of malignant and inflammatory diseases, including those of the gastrointestinal tract (*18–21,28–30*); however, the relationship between ^{18}F-FDG uptake and the condition of gastrointestinal ulceration remains unclear.

Subcutaneous administration of indomethacin, a representative NSAID (10 mg/kg), caused small-intestine ulceration on the mesenteric attachment side, mainly in the ileum, with ulceration almost healed in 1 wk, as previously shown in macro- and microscopic observations reported by Hatazawa et al. (*27*). In the present PET study, we used propofol 4 times (before treatment and on days 1, 2, and 7) to anesthetize each rat. Propofol is known to modulate gamma-aminobutyric acid (GABA)-ergic transmission and exerts its pharmacologic effects by enhancing the function of the GABA-activated chloride channels (*31*). Therefore, we cannot rule out the possibility that feeding behavior and locomotor activity were affected during the experiment. The dose used in this study, however, did not affect the severity or healing of the intestinal ulcers (data not shown).

In the present study, characteristic abdominal ^{18}F-FDG uptake was observed in indomethacin-induced ulceration, with maximum uptake observed 1 d after indomethacin administration. We used SUV to quantify ^{18}F-FDG uptake in the PET study. The mean SUV was approximately 3 times greater in the indomethacin treatment group than in the pretreatment group on day 1 and returned to the pretreatment level on 7 d. This time course of ulceration was also confirmed by γ-counting. Our data showed the ulcerated areas to have an ^{18}F-FDG SUV of 2.16 ± 0.28, compared with 0.70 ± 0.08 for the normal areas ($P < 0.01$). Therefore, a threshold SUV of 1.60 (mean − 2 SDs) could be applied for PET evaluation of tissue suspected of being ulcer-positive. These findings indicated that ^{18}F-FDG PET could evaluate not only the severity but also the process of healing on indomethacin-induced intestinal ulceration. Thus, ^{18}F-FDG PET could be useful for noninvasive detection of gastrointestinal ulcers and in follow-up, even in the clinical cases.

The microautoradiographic study provided an understanding of tissue ^{18}F-FDG accumulation at the cellular level. One day after administration of indomethacin (when the mucosal lesions were most severe), marked ^{18}F-FDG accumulations were observed at the marginal, submucosal, and muscular regions of ulceration. These regions contained many peroxidase-positive cells, suggesting that ^{18}F-FDG accumulated in inflammatory cells such as neutrophils and macrophages. On day 4, the number of peroxidase-positive inflammatory cells decreased, and granulation tissue was formed on the ulcer bed. Accumulation of ^{18}F-FDG was found in the granulation tissue. The microautoradiographic study, combined with immunohistochemistry, revealed that ^{18}F-FDG accumulation was observed in α-SMA–positive

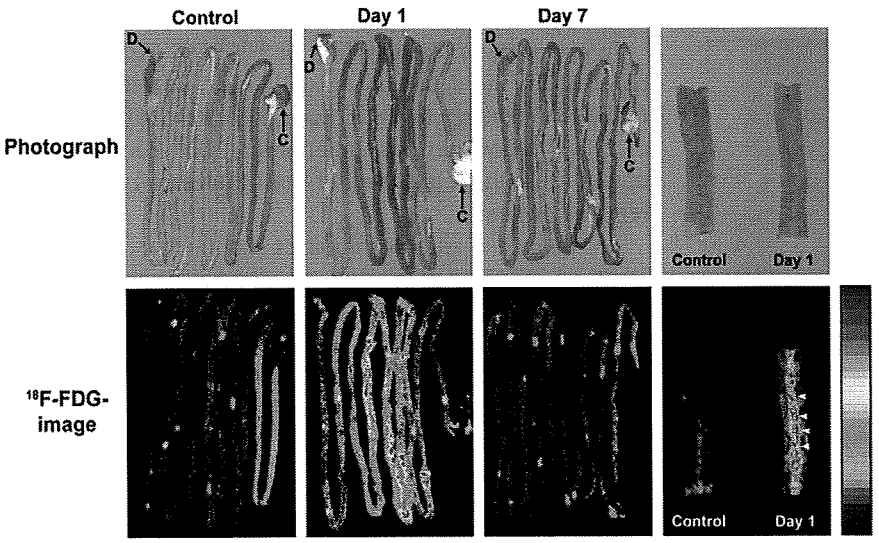

FIGURE 4. ^{18}F-FDG macroautoradiography of intestinal ulceration. Rats were intravenously injected with ^{18}F-FDG and euthanized 45 min later. Discontinuous dotlike ^{18}F-FDG accumulation was clearly identified mainly in ileum on day 1. ^{18}F-FDG imaging profile was similar to that of control on day 7. Images at far right show plain photograph (upper) and ^{18}F-FDG image (lower) of intestines opened along longitudinal axis for control and at day 1. D = duodenum; C = cecum.

myofibroblasts, CD31-positive endothelial cells, and a few ED2-positive macrophages.

Myofibroblasts are thought to play an important role in the repair of injured gut (*32,33*); contraction of intestinal myofibroblasts rapidly reduces mucosal defects and decreases the area requiring reepithelialization (*33*). CD31-immunopositive endothelial cells are also well known to play an important role in ulcer healing by angiogenesis (*34,35*). Kubota et al. (*36*) reported that ^{18}F-FDG accumulation in macrophages and neutrophils likely occurred via the use of glucose as the energy source for their chemotaxis and phagocytosis and in fibroblasts for proliferation in and around tumors, although those ^{18}F-FDG–accumulated cells were not identified immunohistochemically. These observations support the findings of the present study obtained by microautoradiography combined with immunohistochemical identification of cells.

In addition to cells with accumulated ^{18}F-FDG, we found that cells located in deeper regions of the intestinal crypts, and in normal tissue, were heavily radiolabeled with ^{18}F-FDG. The combination study of ^{18}F-FDG microautoradiography with immunohistochemistry revealed that the cells were immunopositive for Ki67. Such regions of the intestinal crypts are known to contain many intestinal stem cells expressing Ki67 (*37*). The stem cells actively proliferate and differentiate mainly into absorptive cells, the major constituent of the epithelial cells of the villus, migrating upward along the crypt-villus axis (*38,39*). These findings indicate that proliferating cells in the intestinal epithelium actively take up ^{18}F-FDG. Ki67 is known to be included in the granular components of the nucleolus during late G1, S, G2, and M phases (*40*); therefore, additional studies using cell cycle markers are required to understand the relationship between each cell cycle phase and glucose utility. To the best of our knowledge, the present study is the first to show ^{18}F-FDG uptake at the single-cell level by a combination of microautoradiography and immunohistochemistry. Our results indicated that ^{18}F-FDG accumulates in such inflammatory cells during the acute phase of mucosal ulceration and also in the cells forming granulation during the healing phase.

NSAIDs, some of the most commonly prescribed drugs worldwide for antipyresis and analgesia, act by inhibition of endogenous prostaglandin synthesis. Prostaglandins are well known to maintain the mucosal integrity of the gastrointes-

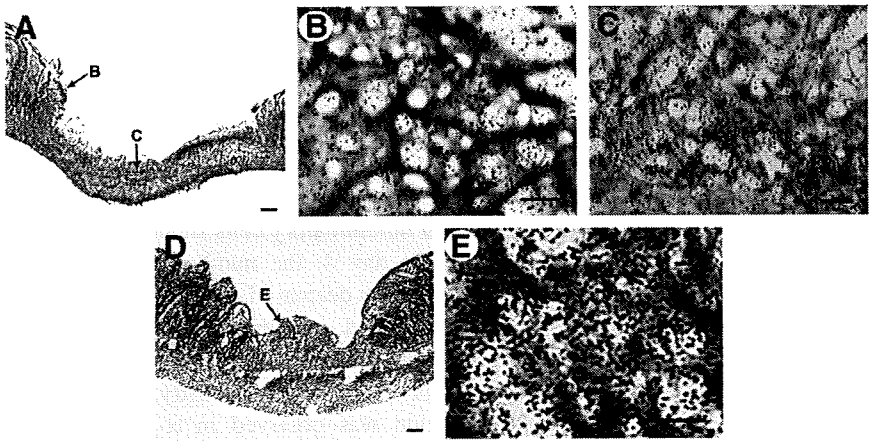

FIGURE 5. ^{18}F-FDG microautoradiography of indomethacin-induced intestinal lesions combined with hematoxylin and eosin staining. (A–C) At 1 d after administration of indomethacin, silver grains of high density were observed in ulcerated area, especially at ulcer margin (B) and submucosal and smooth muscle layer (C). B and C are magnified views of areas indicated by arrows B and C in A. (D and E) On day 4, grains were accumulated on cells forming granulation tissue. (E) Magnified view of the region indicated by arrow E in D. Scale bars: 100 μm (A and D) and 20 μm (B, C, and E).

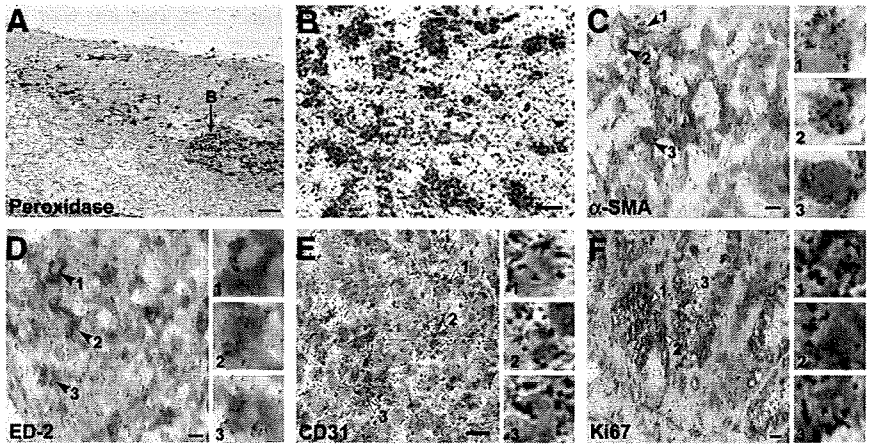

FIGURE 6. Microautoradiography combined with immunohistochemistry. In submucosal area at day 1 after indomethacin administration, ^{18}F-FDG uptake was observed mainly in peroxidase-positive cells (A and B). On granulation tissue at day 4, myofibroblasts (C; α-SMA–positive), macrophages (D; ED2-positive), and endothelial cells (E; CD31-positive) were visualized. In normal tissue, silver grains of high density reflecting ^{18}F-FDG radioactivity were observed in Ki67-positive crypt cells (F). Insets show magnified view of region indicated by arrowheads in each panel. Scale bars: 100 μm (A), 10 μm (B), and 5 μm (C–F).

tinal tract; therefore, NSAIDs commonly cause gastrointestinal damage as an adverse effect. The recently developed technique of capsule enteroscopy has enabled examination of damage to the small bowel and is now considered the gold standard for diagnosis of Crohn disease of the intestine (*4,5*). However, in this technique, the images are magnified to differing extents depending on the amount of surrounding fluid, making it difficult to evaluate lesion size (*7*). Furthermore, capsule enteroscopy carries a risk of capsule retention if there is obstruction of the digestive tract, which may occur in intestinal disorders. In the present study, we demonstrated the usability of ^{18}F-FDG PET and also the meaning of physiologic and pathologic glucose uptake for indomethacin-induced intestinal ulceration. Because ^{18}F-FDG PET is used clinically for diagnosis of cancer or tumors and has low adverse effects, the safety of the method for patients is well established. Clinical studies are needed to evaluate whether ^{18}F-FDG PET exhibits sufficient sensitivity and specificity for the detection of indomethacin-induced small-intestine ulcers in humans. ^{18}F-FDG PET will enable detection of intestinal lesions, staging of disease, and assessment of clinical treatment and reveal recurrence of disease.

CONCLUSION

Our experimental data suggest that ^{18}F-FDG PET may be useful for evaluating indomethacin-induced small-intestine ulcers. ^{18}F-FDG accumulation was observed mainly in inflammatory cells in the acute phase and in myofibroblasts and endothelial cells forming granulation tissue in the healing phase. PET enables detection of accumulation during the course of ulceration.

ACKNOWLEDGMENTS

We thank the staff of Osaka City University Hospital for ^{18}F-FDG synthesis and provision; the staff of the radioisotope center, Osaka City University Graduate School of Medicine, for their cooperation; Kaori Okuyama for technical assistance; and Dr. Annabel Boyes for the editorial help.

This work was supported by a consignment expense for the Molecular Imaging Program on Research Base for Exploring New Drugs from the Ministry of Education, Culture, Sports, Science and Technology (MEXT), Japanese government.

REFERENCES

1. Robert A, Asano T. Resistance of germ-free rats to indomethacin-induced intestinal inflammation. *Prostaglandins.* 1977;14:333–341.
2. Fang WF, Broughton A, Jacobson ED. Indomethacin induced intestinal inflammation. *Am J Dig Dis.* 1977;22:749–760.
3. Bjarnason I, Zanelli G, Smith T, et al. Nonsteroidal anti-inflammatory drug-induced intestinal inflammation in humans. *Gastroenterology.* 1987;93:480–489.
4. Marmo R, Rotondano G, Piscopo R, et al. Capsule endoscopy versus enteroclysis in the detection of small-bowel involvement in Crohn's disease: a prospective trial. *Clin Gastroenterol Hepatol.* 2005;3:772–776.
5. Girelli CM, Porta P, Malacrida V, Barzaghi F, Rocca F. Clinical outcome of patients examined by capsule endoscopy for suspected small bowel Crohn's disease. *Dig Liver Dis.* 2007;39:148–154.
6. Graham DY, Opekun AR, Willingham FF, Qureshi WA. Visible small-intestinal mucosal injury in chronic NSAID users. *Clin Gastroenterol Hepatol.* 2005;3:55–59.
7. Maiden L, Thjodleifsson B, Theodors A, Gonzalez J, Bjarnason I. A quantitative analysis of NSAID-induced small bowel pathology by capsule enteroscopy. *Gastroenterology.* 2005;128:1172–1178.
8. Dang CV, Semenza GL. Oncogenic alterations of metabolism. *Trends Biochem Sci.* 1999;24:68–72.
9. Gambhir SS, Czernin J, Schwimmer J, Silverman DH, Coleman RE, Phelps ME. A tabulated summary of the FDG PET literature. *J Nucl Med.* 2001;42(5 suppl): 1S–93S.
10. Price P. Changes in ^{18}F-FDG uptake measured by PET as pharmacodynamic endpoint in anticancer therapy: how far have we got? *Br J Cancer.* 2000;83:281–283.
11. McKeehan WL. Glycolysis, glutaminolysis and cell proliferation. *Cell Biol Int Rep.* 1982;6:635–650.
12. Weber G, Morris HP, Love WC, Ashmore J. Comparative biochemistry of hepatomas. II. Isotope studies of carbohydrate metabolism in Morris hepatoma 5123. *Cancer Res.* 1961;21:1406–1411.
13. Weber G. Enzymology of cancer cells. *N Engl J Med.* 1977;296:541–551.
14. Bakheet SM, Saleem M, Powe J, Al-Amro A, Larsson SG, Mahassin Z. F-18 fluorodeoxyglucose chest uptake in lung inflammation and infection. *Clin Nucl Med.* 2000;25:273–278.
15. Hustinx R, Smith RJ, Benard F, et al. Dual time point fluorine-18 fluorodeoxyglucose positron emission tomography: a potential method to differentiate malignancy from inflammation and normal tissue in the head and neck. *Eur J Nucl Med.* 1999;26:1345–1348.
16. Shreve PD. Focal fluorine-18 fluorodeoxyglucose accumulation in inflammatory pancreatic disease. *Eur J Nucl Med.* 1998;25:259–264.
17. Ichiya Y, Kuwabara Y, Sasaki M, et al. FDG-PET in infectious lesions: the detection and assessment of lesion activity. *Ann Nucl Med.* 1996;10:185–191.
18. Bicik I, Bauerfeind P, Breitbach T, von Schulthess GK, Fried M. Inflammatory bowel disease activity measured by positron-emission tomography [abstract]. *Lancet.* 1997;350:262.

19. Neurath MF, Vehling D, Schunk K, et al. Noninvasive assessment of Crohn's disease activity: a comparison of ^{18}F-fluorodeoxyglucose positron emission tomography, hydromagnetic resonance imaging, and granulocyte scintigraphy with labeled antibodies. *Am J Gastroenterol.* 2002;97:1978–1985.
20. Lemberg DA, Issenman RM, Cawdron R, et al. Positron emission tomography in the investigation of pediatric inflammatory bowel disease. *Inflamm Bowel Dis.* 2005;11:733–738.
21. Louis E, Ancion G, Colard A, Spote V, Belaiche J, Hustinx R. Noninvasive assessment of Crohn's disease intestinal lesion with ^{18}F-FDG PET/CT. *J Nucl Med.* 2007;48:1053–1059.
22. Brewer S, McPherson M, Fujiwara D, et al. Molecular imaging of murine intestinal inflammation with 2-deoxy-2-[^{18}F]fluoro-D-glucose and positron emission tomography. *Gastroenterology.* 2008;135:744–755.
23. Krawisz JE, Sharon P, Stenson WF. Quantitative assay for acute intestinal inflammation based on myeloperoxidase activity: assessment of inflammation in rat and hamster models. *Gastroenterology.* 1984;87:1344–1350.
24. Hamacher K, Coenen HH, Stocklin G. Efficient stereospecific synthesis of no-carrier-added 2-[^{18}F]-fluoro-2-deoxy-D-glucose using aminopolyether supported nucleophilic substitution. *J Nucl Med.* 1986;27:235–238.
25. Matsumura A, Mizokawa S, Tanaka M, et al. Assessment of microPET performance in analyzing the rat brain under different types of anesthesia: comparison between quantitative data obtained with microPET and ex vivo autoradiography. *Neuroimage.* 2003;20:2040–2050.
26. Kubota R, Yamada S, Kubota K, Ishiwata K, Tamahashi N, Ido T. Intratumoral distribution of fluorine-18-fluorodeoxyglucose in vivo: high accumulation in macrophages and granulation tissues studied by microautoradiography. *J Nucl Med.* 1992;33:1972–1980.
27. Hatazawa R, Ohno R, Tanigami M, Tanaka A, Takeuchi K. Roles of endogenous prostaglandins and cyclooxygenase isozymes in healing of indomethacin-induced small intestinal lesions in rats. *J Pharmacol Exp Ther.* 2006;318:691–699.
28. Annovazzi A, Peeters M, Maenhout A, Signore A, Dierckx R, Van De Wiele C. 18-fluorodeoxyglucose positron emission tomography in nonendocrine neoplastic disorders of the gastrointestinal tract. *Gastroenterology.* 2003;125:1235–1245.
29. Chin BB, Wahl RL. ^{18}F-Fluoro-2-deoxyglucose positron emission tomography in the evaluation of gastrointestinal malignancies. *GUT.* 2003;52(suppl 4): 23–29.
30. Kresnik E, Gallowitsch HJ, Mikosch P, et al. ^{18}F-FDG positron emission tomography in the early diagnosis of enterocolitis: preliminary results. *Eur J Nucl Med Mol Imaging.* 2002;29:1389–1392.
31. Concas A, Santoro G, Mascia MP, Serra M, Sanna E, Biggio G. The general anesthetic propofol enhances the function of gamma-aminobutyric acid-coupled chloride channel in the rat cerebral cortex. *J Neurochem.* 1990;55:2135–2138.
32. Powell DW, Adegboyega PA, Di Mari JF, Mifflin RC. Epithelial cells and their neighbors. I. Role of intestinal myofibroblasts in development, repair and cancer. *Am J Physiol Gastrointest Liver Physiol.* 2005;289:G2–G7.
33. Powell DW, Mifflin RC, Valentich JD, Crowe SE, Saada JI, West AB. Myofibroblasts. II. Intestinal subepithelial myofibroblasts. *Am J Physiol.* 1999;277: C183–C201.
34. DeLisser HM, Christofidou-Solomidou M, Strieter RM, et al. Involvement of endothelial PECAM-1/CD31 in angiogenesis. *Am J Pathol.* 1997;151:671–677.
35. Hudson N, Balsitis M, Everitt S, Hawkey CJ. Angiogenesis in gastric ulcers: impaired in patients taking non-steroidal anti-inflammatory drugs. *Gut.* 1995; 37:191–194.
36. Kubota K, Kubota R, Yamada S. FDG accumulation in tumor tissue. *J Nucl Med.* 1993;34:419–421.
37. Qiu JM, Roberts SA, Potten CS. Cell migration in the small and large bowel shows a strong circadian rhythm. *Epithelial Cell Biol.* 1994;3:137–148.
38. Stappenbeck TS, Wong MH, Saam JR, Mysorekar IU, Gordon JI. Notes from some crypt watchers: regulation of renewal in the mouse intestinal epithelium. *Curr Opin Cell Biol.* 1998;10:702–709.
39. Brittan M, Wright NA. Stem cell in gastrointestinal structure and neoplastic development. *Gut.* 2004;53:899–910.
40. Schluter C, Duchrow M, Wohlenberg C, et al. The cell proliferation-associated antigen of antibody Ki-67: a very large, ubiquitous nuclear protein with numerous repeated elements, representing a new kind of cell cycle-maintaining proteins. *J Cell Biol.* 1993;123:513–522.

^{11}C-PK11195 PET for the In Vivo Evaluation of Neuroinflammation in the Rat Brain After Cortical Spreading Depression

Yilong Cui[1], Tadayuki Takashima[2], Misato Takashima-Hirano[3], Yasuhiro Wada[2], Miho Shukuri[4], Yasuhisa Tamura[1], Hisashi Doi[3], Hirotaka Onoe[4], Yosky Kataoka[1], and Yasuyoshi Watanabe[2]

[1]Cellular Function Imaging Laboratory, RIKEN Center for Molecular Imaging Science, Kobe, Hyogo, Japan; [2]Molecular Probe Dynamics Laboratory, RIKEN Center for Molecular Imaging Science, Kobe, Hyogo, Japan; [3]Molecular Imaging Labeling Chemistry Laboratory, RIKEN Center for Molecular Imaging Science, Kobe, Hyogo, Japan; and [4]Functional Probe Research Laboratories, RIKEN Center for Molecular Imaging Science, Kobe, Hyogo, Japan

Neurogenic inflammation triggered by extravasation of plasma protein has been hypothesized as a key factor in the generation of the pain sensation associated with migraine. The principal immune cell that responds to this inflammation is the parenchymal microglia of the central nervous system. **Methods:** Using a PET technique with ^{11}C-(*R*)-[1-(2-chlorophenyl)-*N*-methyl-*N*-(1-methylpropyl)-3-isoquinolinecarboxamide] (^{11}C-PK11195), a PET ligand for peripheral type–benzodiazepine receptor, we evaluated the microglial activation in the rat brain after generation of unilateral cortical spreading depression, a stimulation used to bring up an experimental animal model of migraine. **Results:** We found a significant increase in the brain uptake of ^{11}C-PK11195, which was completely displaceable by the excess amounts of unlabeled ligands, in the ipsilateral hemisphere of the spreading depression–generated rats. Moreover, the binding potential of ^{11}C-PK11195 in the spreading depression–generated rats was significantly higher than that in the sham-operated control rats. **Conclusion:** These results suggest that as an inflammatory reaction, microglial cells are activated in response to the nociceptive stimuli induced by cortical spreading depression in the rat brain. Therefore, the ^{11}C-PK11195 PET technique could have a potential for diagnostic and therapeutic monitoring of neurologic disorders related to neuroinflammation such as migraine.

Key Words: binding potential; microglia; peripheral benzodiazepine receptor; migraine

J Nucl Med 2009; 50:1904–1911
DOI: 10.2967/jnumed.109.066498

Neuroinflammation is a process whereby glial cells are activated in response to infection, disease, or injuries involved in the central nervous system. Such inflammatory reactions are implicated in several neurologic disorders such as migraine, Alzheimer disease, stroke, Parkinson disease, brain trauma, spinal cord injury, and multiple sclerosis (*1,2*). Neurogenic inflammation has been implicated as a key factor in the generation of the pain sensation associated with migraine headaches (*3–5*). It is hypothesized that the proinflammatory peptides, such as substance P and calcitonin gene–related peptide, released from trigeminocervical nerve terminals in response to meningeal nociceptive stimuli, induce vasodilation and plasma protein extravasation. Such neurogenic inflammatory reactions were thought to trigger headache via a stimulation of trigeminal afferents (*4,5*). Consistent with this theory, vasogenic leakage (*6,7*) and an increase in calcitonin gene–related peptide in the jugular vein (*8*) have been reported in migraine patients during migraine attack. However, recent clinical trials have shown that several drugs that selectively inhibit plasma protein extravasation in rodents have failed to reduce pain severity in patients with migraine (*9*). These observations indicate that a noninvasive evaluation method for neuroinflammation is necessary to investigate whether and how the neuroinflammation is involved in migraine etiology and verify the extrapolated data from an animal study to the human condition.

As the principal immune cells in the central nervous system, the microglial cells are activated in response to such neurogenic inflammation. The process of microglial activation is thought to be related to an increase in the number of microglial cells and the expression of numerous proteins such as peripheral benzodiazepine receptor (PBR) (*10*). The PBR, which is a mitochondrial outer membrane protein and is expressed at low levels in the normal brain on resting microglial cells and astrocytes, is known to be upregulated in the activated microglial cells (*11–13*). ^{11}C-labeled PK11195, a ligand that specifically binds to PBR, has been used extensively for imaging of activated microglial cells by PET in several neurologic disorders, such as stroke (*14*), multiple sclerosis (*15*), Alzheimer disease (*16*), Parkinson disease (*17*), and Huntington disease (*18*). However, no literature has described the

Received May 22, 2009; revision accepted Aug. 17, 2009.
Correspondence or reprints contact: Yilong Cui, Cellular Function Imaging Laboratory, RIKEN Center for Molecular Imaging Science, 6-7-3 Minatojima Minamimachi, Chuo-ku, Kobe, Hyogo 650-007, Japan.
E-mail: cuiyl@riken.jp

microglial activation in the brain of migraine patients using PET with ^{11}C-PK11195.

Cortical spreading depression, described first by Leao (*19*) in 1944, is implicated in the pathogenesis of migraine. Cortical spreading depression is characterized by the spreading of neuronal or glial membrane depolarization accompanied by temporal elevation of the cerebral blood flow (CBF) throughout the cerebral cortical hemisphere at a rate of 2–5 mm/min (*20,21*). The rate of spread correlates with the observed spread of the aura of classic migraine (*22*), which is characterized by either a paracentral scotoma or a small scintillating area of bright light. A spreading oligemia has been observed at a similar velocity during migraine attacks in experimental cortical spreading depression models (*23,24*). Hadjikhani et al. (*25*) also reported that a neurovascular event closely resembling cortical spreading depression has been shown with functional MRI during the migraine visual aura. On the basis of these observations and other experimental data, the cortical spreading depression has been hypothesized as an endogenous event involved in migraine etiology (*26,27*). In this study, we used ^{11}C-PK11195 PET to investigate the neurogenic inflammation in the cerebral cortex induced by unilateral cortical spreading depression.

MATERIALS AND METHODS

All experimental protocols were approved by the Ethics Committee on Animal Care and Use of the Institute of Physical and Chemical Research and were performed in accordance with the *Guide for the Care and Use of Laboratory Animals* (*28*).

Chemicals

(*R*)-[1-(2-chlorophenyl)-*N*-methyl-*N*-(1-methyl-propyl)-3-isoquinoline-carboxamide] ((*R*)-*N*-desmethyl-PK11195) was obtained from Advanced Biochemical Compounds (ABX). ^{11}C-labeled PK11195 was synthesized according to the procedures described by Shah et al. (*29*), with slight modifications. Briefly, 1 mg of (*R*)-*N*-desmethyl-PK11195 was dissolved in 200 μL of anhydrous dimethyl sulfoxide, containing 1 mg of KOH. After trapping of the ^{11}C-CH_3I, the vial was heated at 90°C for 4 min. Purification was performed by high-performance liquid chromatography on a COSMOSIL C_{18}-AR-II column (10 × 250 mm, 5-μm particle size) (Nakalai) using acetonitrile:water (70:30) as the mobile phase. The purified fraction was evaporated to dryness and reconstituted with 4 mL of a saline solution including 0.3 mL of propylene glycol and 0.05 mL of polysorbate 80. The specific activity ranged from 30 to 70 GBq/μmol. Radiochemical purity was higher than 99%.

Animal Preparation for Generation of Spreading Depression

Male Sprague–Dawley rats (SLC), weighing approximately 300 g, were used. To prepare the spreading depression rat model, the head of each rat was fixed in a stereotactic apparatus (type 1430, David Kopf) under 1.5% isoflurane anesthesia. A thermocouple probe was connected with a thermocontroller and inserted into the rectum to maintain the body temperature at 37°C. A small burr hole was drilled in the skull at the frontal cortex (2.0–3.0 mm anterior and 2.0–3.0 mm lateral to the bregma). A glass micropipette (internal diameter of the tip, 50 μm) was inserted 1 mm below the cortical surface through the burr hole for subsequent microinjection. Two hours after the insertion, a microinjection of 1 M KCl was performed (at a rate of 0.2 μL/min for 1 min) every 10 min for a period of 2 h (12 injections; 2.4 μL of total volume). Sham controls (n = 4 animals) were injected with 1 M NaCl at an analogous rate, duration, and frequency.

A laser Doppler flowmetry (LDF) (type FLO-N1; ω-wave) probe was stereotactically placed in the parietal cortex over the skull for recording changes in CBF. The absolute value from LDF does not mean actual perfusion units; therefore, relative change in CBF is displayed (the data are normalized to prelevel).

PET Studies

Rats (n = 39) were anesthetized and maintained with a mixture of 1.5% isoflurane and nitrous oxide and oxygen (7:3) and positioned in the gantry of a PET scanner (microPET Focus 220; Siemens Co., Ltd.). After a bolus injection of ^{11}C-PK11195 (~100 MBq per animal) via a tail vein, a 60-min emission scan was performed with 400–650 keV as the energy window and 6 ns as the coincidence time window. Unlabeled ligands (n = 4, 1 mg/kg) were injected intravenously 20 min after the injection of radiotracers for the displacement experiment. Emission data were acquired in the list mode. The acquired data were sorted into single sinogram (for static image) and dynamic sinograms (6 × 10 s, 6 × 30 s, 11 × 60 s, and 15 × 180 s, for a total of 38 frames). The data were reconstructed by standard 2-dimensional filtered backprojection (FBP) with ramp filter and cutoff frequency at 0.5 cycles per pixel or by a statistical maximum a posteriori probability (MAP) algorithm (12 iterations with point spread function effect). Compared with FBP, MAP-reconstructed images have been shown to result in improved spatial resolution and noise properties on small-animal PET images, an advantage for image coregistration. Meanwhile, FBP-reconstructed images were used for quantification. The radioactivity concentrations were normalized with cylinder phantom data and were expressed as standardized uptake values.

Image Analysis

A 3-dimensional T2-weighted MRI template, which was aligned in space with the rat brain atlas of Paxinos (*30*), was used for defining regions of interest (ROIs). PET images were manually coregistered with the MRI template using an image-processing small-animal PET software package (ASIPro 6.05; Siemens Co., Ltd.). ROIs were defined for each rat on the region of microinjection (core, as delineated by the hypersignal seen in the MAP-reconstructed image), ipsilateral surrounding areas (ipsilateral), and corresponding contralateral areas (contralateral, as shown in Fig. 1). Each region was primarily drawn on coronal slices and then confirmed on sagittal and horizontal slices. All related ROIs were stacked into the volume of interest (VOI), and the mean value in each VOI was used to generate regional time–activity curves.

Radioactivity and Metabolite Analysis in Plasma

Arterial blood was collected from the femoral artery at 10, 20, 30, 40, 50, and 60 s and 2, 5, 10, 25, and 40 min after administration. The radioactivity of blood and plasma was measured by a well-type γ-counter (Wallac1470; PerkinElmer) and corrected for decay. For the metabolite analysis, plasma

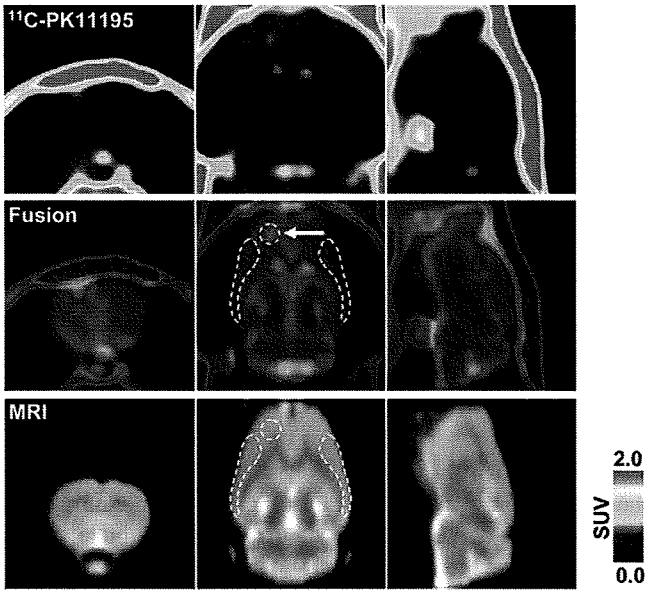

FIGURE 1. Representative ^{11}C-PK11195 PET image coregistered with MRI template 8 d after generation of unilateral (left hemisphere) cortical spreading depression. PET image was reconstructed with MAP algorithm and summated from 5 to 60 min after radioligand injection. Arrow in middle panel indicates KCl-microinjected area (core). White broken lines in middle and bottom panels indicate ROIs (core, ipsilateral, and contralateral, respectively) defined in this study.

samples (1, 2, 5, 10, 25, and 40 min after administration) were extracted by acetonitrile, and the extracts were applied to an RP-18 thin-layer chromatography (TLC) plate (Merck). The plate was developed with acetonitrile:water (70:30) as the mobile phase. After migration, the TLC plates were dried and exposed on imaging plates (BAS TR2040; Fuji Photo Film) for 40 min. The signal of radioactivity on the imaging plates was measured with a digital PSL autoradiography analyzer (FLA-7000; Fuji Photo Film), and the data were estimated using imaging-analysis software (MultiGauge; Fuji Photo Film).

Kinetic Analysis

Kinetic modeling was performed using the PMOD software package (version 2.85; PMOD Technologies). A metabolite-corrected plasma input function was obtained by fitting to an exponential function, as follows. The ^{11}C-PK11195 parent fraction in the plasma samples for each sampling point was multiplied by this exponential function to obtain the metabolite-corrected plasma input function. The metabolite-corrected plasma time–activity curves were fitted to 2 exponential functions to obtain the plasma pharmacokinetic parameter. The standard input function was obtained by averaging individual input functions from 3 satellite rats, and k_2' of the reference region (contralateral hemisphere), which represents the clearance from the reference region into the vascular compartment, was obtained using a 1-tissue-compartment model for each animal imaged. The averaged k_2' estimated in this study was 0.14/min. Binding potential (BP) was calculated for ipsilateral ROI kinetics using Logan noninvasive graphical analysis (*31*), which was applied to the target regions by the following equation:

$$\frac{\int_0^T C(t)dt}{C(T)} = DVR\left[\frac{\int_0^T C'(t)dt + C'(T)/k_2'}{C(T)}\right] + int',$$

where $C(T)$ is the radioactivity concentration in the tissue of interest, and $C'(T)$ is the radioactivity concentration in the reference tissue (contralateral ROI). DVR is the distribution volume ratio calculated by the regression slope, int′ is an intercept that becomes constant after an equilibration, and k_2' is the average tissue-to-plasma clearance, which has to be determined before this analysis. In this study, k_2' was determined directly using the standard input function as shown above. Finally, BP is evaluated as BP = DVR − 1.

Immunohistochemistry

The level of microglial activation was investigated by immunohistochemistry in the spreading depression–generated (n = 4) and sham control (n = 4) rats at 8 d after the operation. After the PET scan, the rats were anesthetized and perfused with 4% formaldehyde buffered with 0.1 M phosphate-buffered saline (pH 7.4). The brain was removed and further fixed in the same fixative at 4°C for 24 h. We prepared coronal brain sections (30-μm thickness) using a cryostat. To immunostain the microglial cells, mouse monoclonal antibody against rat OX-42 (1:100; Abcam) was used. The bound antibodies were visualized by the avidin–biotin complex method (Vectastain ABC kit; Vector) with 3, 3′-diaminobenzidine.

Data Analysis

All results were expressed as mean ± SD. The statistical differences in BP values between spreading depression–generated and sham-operated groups were assessed by 2-tailed unpaired t test. The statistical significance was set at P less than 0.05.

RESULTS

Spreading Depression in Rat Cerebral Cortex

Occurrence of cortical spreading depression in all rats used for the PET study was evaluated by transient CBF hyperperfusion recorded continuously from the ipsilateral hemisphere (7 mm posterior to the injection site). Transient CBF hyperperfusion always occurred after microinjection of 1 M KCl (at a rate of 0.2 μL/min for 1 min) in the ipsilateral hemisphere (Fig. 2), as is characteristic of spreading depression (*21*). Such transient CBF hyperperfusions are well known to be synchronously accompanied by the transient negative shifts of direct current (DC) potential, as described in our previous report (*21*) and in other literature (*32*). The mean number of transient hyperperfusions in the KCl-treated rats (n = 35) was 12.8 ± 3.3 over 2 h. However, microinjection of 1 M NaCl (n = 4) in an analogous fashion did not induce similar changes in CBF, indicating that cortical spreading depression was not induced in those rats.

PET Studies

To investigate the neurogenic inflammation after cortical spreading depression, we examined microglial activation using ^{11}C-PK11195 PET at 1, 3, 8, and 15 d after induction

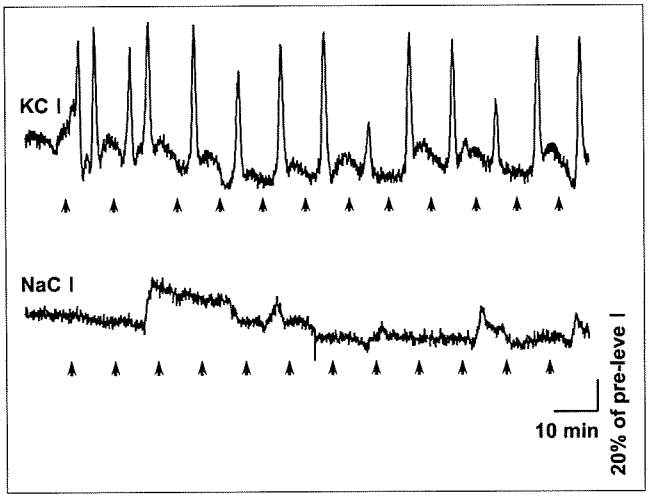

FIGURE 2. Cortical spreading depression–associated CBF changes in experimental and sham-operated rat. Dynamic changes in CBF were continuously recorded from parietal cortex over skull using LDF. Upper panel shows a representative CBF change recorded from parietal cortex in KCl-microinjected rat. Lower panel shows result from a rat who received NaCl microinjection using analogous paradigm, as sham operation. Arrows at bottom of each panel indicate time of microinjection. Note that spreading depression–associated CBF hyperperfusions were not observed in sham-operated rat.

of unilateral cortical spreading depression in the rats. The radioactivity of ^{11}C-PK11195 was barely observed within the brain under normal condition in the control rats, except for the cerebral ventricles, including the lateral ventricle, third ventricle, and fourth ventricle (data not shown). In the cortical spreading depression–generated rats, ^{11}C-PK11195 radioactivity was high in the ipsilateral hemisphere, as compared with that in the contralateral hemisphere. The ^{11}C-PK11195 radioactivity was detectable in the injection site 1 d after the KCl treatment, and that increased and spread extensively in the ipsilateral surrounding areas at 3, 8, and 15 d after the KCl treatment (Figs. 1 and 3). Figure 1 shows a representative ^{11}C-PK11195 PET image coregistered with the corresponding MR image at 8 d after the KCl treatment. The highest radioactivity was seen in the KCl-microinjected site (core), and moderate radioactivity was observed in the ipsilateral surrounding areas but not in the corresponding contralateral areas (Fig. 1). In the sham control rats, however, a slight increase in ^{11}C-PK11195 radioactivity was seen primarily in the NaCl-microinjected site at 8 d after the sham operation.

The temporal changes of ^{11}C-PK11195 uptake in the core, ipsilateral, and contralateral ROIs were similar (Fig. 3). The radioactivity of ^{11}C-PK11195 in the contralateral ROI reached a peak within the first minute after radiotracer injection and decreased rapidly thereafter. In the cortical spreading depression–generated rats, the decrement in the ipsilateral areas (core and ipsilateral ROIs) was slower than that in the contralateral areas (contralateral ROI). The obvious contrast of radioactivity between ipsi- and contralateral hemispheres appeared first 3 d after the operation and remained until the end of the study (Fig. 3). No obvious contrast between the 2 hemispheres was observed in the sham-operated control rats at 8 d after the NaCl treatment.

In vivo displacement was performed by injecting unlabeled PK11195 (n = 4, 1 mg/kg) at 20 min after the injection of ^{11}C-PK11195 (Fig. 4). Immediately after injection of unlabeled PK11195, the brain uptake of ^{11}C-PK11195 was transiently increased in both ipsi- and contralateral hemispheres because of a release of ^{11}C-PK11195 from peripheral organs into the blood circulation, as previously reported (*33,34*). The contrast of radioactivity between the 2 hemispheres completely disappeared after the unlabeled PK11195 injection, indicating ^{11}C-PK11195 was rapidly displaced by unlabeled PK11195 in the ipsilateral hemisphere.

Using Logan noninvasive graphical analysis, we estimated the BP value for ^{11}C-PK11195 in the core and ipsilateral ROIs. The BP values in the core and ipsilateral ROIs were increased with the time after the KCl treatment (Fig. 5). In the cortical spreading depression–generated rats, the mean value of BP in the core ROI reached 0.45 ± 0.10 (n = 5) at 3 d after the KCl treatment and maintained approximately the same level until 15 d (0.51 ± 0.36, n = 5). The mean values in the ipsilateral ROI were approximately half of those in the core ROI at each time of the examination, indicating that microglial activation was outstanding in the microinjected site. In contrast with the cortical spreading depression–generated rats, the BP values were lower in the sham-operated control (NaCl treatment) rats. Significant differences between spreading depression–generated and sham control rats were noted in both ROIs at 8 d after the operation (core, 0.48 ± 0.18 vs. 0.21 ± 0.05, and ipsilateral, 0.26 ± 0.07 vs. 0.14 ± 0.08, in the spreading depression–generated [n = 11] and sham control [n = 4] rats, respectively; $P < 0.05$, unpaired t test) (Fig. 6).

Immunohistochemical Studies

The activation of microglial cells was confirmed by immunohistochemical studies after the induction of spreading depression. As shown in Figure 7, a large number of immunosignals of OX-42 were observed in the ipsilateral hemisphere, compared with the corresponding area of the contralateral hemisphere, in the rats 8 d after unilateral spreading depression generation. Magnified photomicrographs taken from the corresponding parietal cortex showed that hypertrophied (enlarged, darkened soma with shorter, thicker processes) or ameboid (densely stained, enlarged soma with a few short processes) OX-42–positive microglial cells were often seen in the ipsilateral hemisphere (Fig. 7C). However, such a difference between the 2

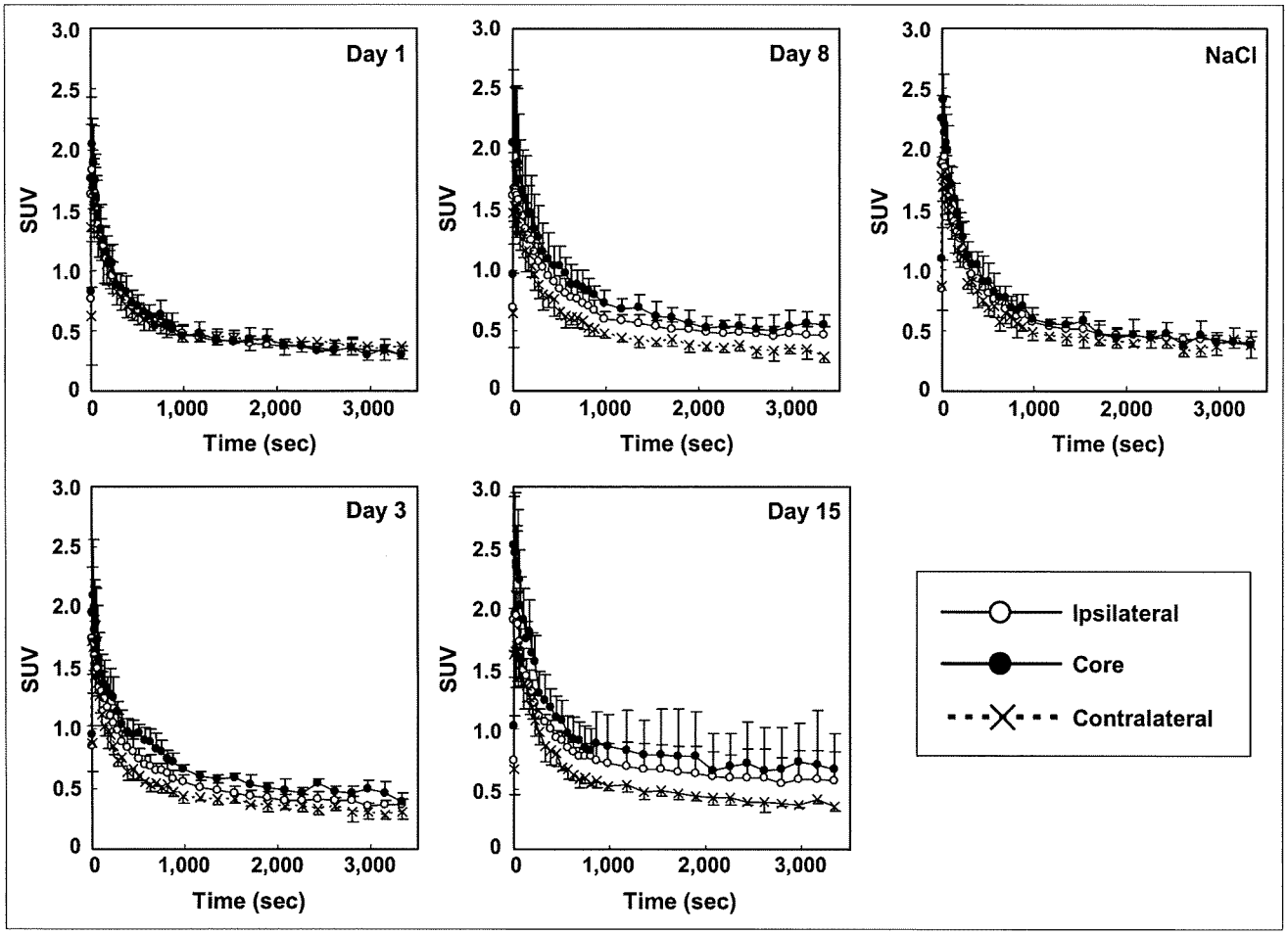

FIGURE 3. Time–activity curves for ^{11}C-PK11195 in brain regions of experimental (at 1, 3, 8, and 15 d after microinjection of KCl) and sham-operated (8 d after microinjection of NaCl) rats. Data were expressed as mean ± SD.

hemispheres was not observed in the rats treated with NaCl as a sham operation.

DISCUSSION

Neurogenic inflammation is thought to be a key factor in the generation of pain sensation in migraine headaches. In the present study, we evaluated neurogenic inflammation using an animal model of migraine and noninvasive PET. Our results show that in the unilateral spreading depression model rats, the uptake of ^{11}C-PK11195, a PET tracer for PBR, which is used extensively to image activated microglial cells in the central nervous system, was increased in the ipsilateral hemisphere and completely displaced by excess unlabeled ligands. In addition, quantitative analysis in spreading depression model rats, compared with that in the sham-operated control rats, showed that the BP values in the core and ipsilateral ROIs were significantly high. Finally, predominant microglial activation in the ipsilateral cerebral hemisphere of the spreading depression model rats was also confirmed by immunohistochemical study. These observations suggest that an inflammatory process may be involved in the pathologic state of migraine and that ^{11}C-PK11195 PET is a useful tool for evaluating the neurogenic inflammation in vivo.

On the basis of the expression pattern of the PBR in the pathophysiologic state, ^{11}C-labeled PK11195 has been developed as a specific PET ligand for the PBR to image activated microglial cells in the brain (*15,17,35,36*). The PBR is known to be highly expressed in activated microglial cells under neuropathologic conditions but barely expressed in healthy brain tissue (*12,13*). The upregulated level of PBR was known to be well correlated with the state of microglial activation (*15,37,38*). In the present study, we used unilateral cortical spreading depression as an animal model of migraine and demonstrated that the brain uptake of ^{11}C-PK11195 was specifically increased in the ipsilateral hemisphere. It is well known that cortical spreading depression–induced pathophysiologic changes, such as transient CBF hyperperfusion, negative DC potential shifts, and related biochemical events, are restricted to the ipsilateral hemisphere (*19,21,39*). Consistent with these characteristics of spreading depression, we demonstrated that micro-

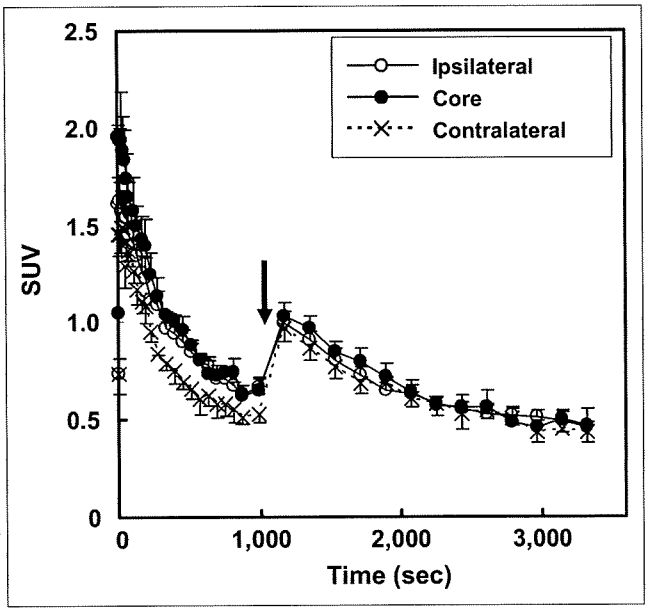

FIGURE 4. Time–activity curves for ^{11}C-PK11195 displaced by excess unlabeled PK11195 in brain regions 8 d after generation of unilateral cortical spreading depression. Unlabeled PK11195 (n = 4, 1 mg/kg) was administered 20 min after injection of radioligand. Arrow indicates time of injection of unlabeled ligand. Data were expressed as mean ± SD.

glial reactivity, indicated by immunosignal of OX-42, was observed predominantly in the ipsilateral hemisphere after cortical spreading depression. Indeed, Caggiano et al. (*40*) have also reported that reactive microglial cells appeared predominantly in the ipsilateral hemisphere after KCl-induced unilateral neocortical spreading depression by the immunohistochemical approach. Moreover, our displacement experiment demonstrated that such a superior brain

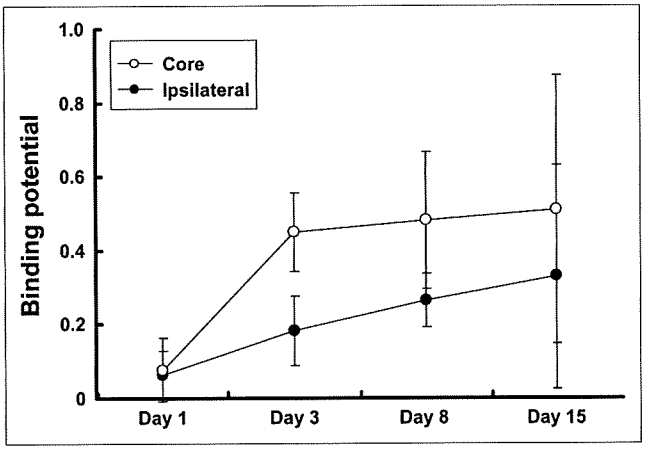

FIGURE 5. BP for ^{11}C-PK11195 in core and ipsilateral ROIs at 1, 3, 8, and 15 d after induction of unilateral cortical spreading depression by KCl microinjection. BP values were estimated in core and ipsilateral ROIs using Logan noninvasive graphical analysis. Corresponding contralateral ROI was used as reference. Data were expressed as mean ± SD.

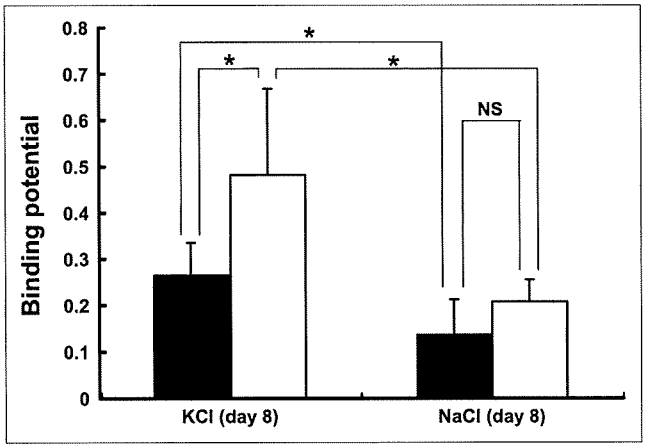

FIGURE 6. Comparison of BP for ^{11}C-PK11195 in ROIs (core and ipsilateral) between experimental and sham-operated rats. BP values were estimated from experimental (KCl microinjection, n = 11) and sham-operated (NaCl microinjection, n = 4) rats 8 d after operation. Open and closed bars indicate core and ipsilateral ROIs, respectively. Data were expressed as mean ± SD. NS = not significant. *$P < 0.05$, unpaired t test.

uptake of ^{11}C-PK11195 in the ipsilateral hemisphere was completely displaced by excess unlabeled ligands. Though astrocytes have also been reported to express PBR in vitro (*41*), the origin of ^{11}C-PK11195 radioactivity in vivo is thought to be primarily from activated microglial cells in the brain (*15,35,36*). Therefore, the increased radioactivity of ^{11}C-PK11195 in the ipsilateral hemisphere may originate from the activated microglial cells in response to the neurogenic inflammation after the unilateral spreading depression.

In the present study, BP value for ^{11}C-PK11195 was estimated using the Logan noninvasive graphical analysis (*31*). The mean BP value for ^{11}C-PK11195 was approximately 0.5 in the core ROI after spreading depression generation. That value was slightly lower than that reported in the α-amino-3-hydroxy-5-methyl-4-isoxazole propionic acid–induced lesion area of the rat striatum (0.66 ± 0.15), in which the BP value was estimated by a simplified reference tissue model (*33*). Using the simplified reference tissue model, Cagnin et al. also have reported that mean BP value for ^{11}C-PK11195 in the cerebral cortex of healthy volunteers was 0.13 ± 0.04 and increased variably (≤0.79) in several cortical regions of patients with herpes simplex encephalitis (*36*). In the present study, the highest value of mean BP for ^{11}C-PK11195 was noted in the KCl-microinjected site (0.48 ± 0.18), and a moderate value was observed in the surrounding area of the injection site (0.26 ± 0.07) 8 d after the unilateral spreading depression generation. In contrast, the BP value in the ipsilateral hemisphere of sham-operated rats was 0.14 ± 0.08, which was almost equivalent to the value reported by Cagnin et al. for the cerebral cortex of healthy volunteers. (*36*). These

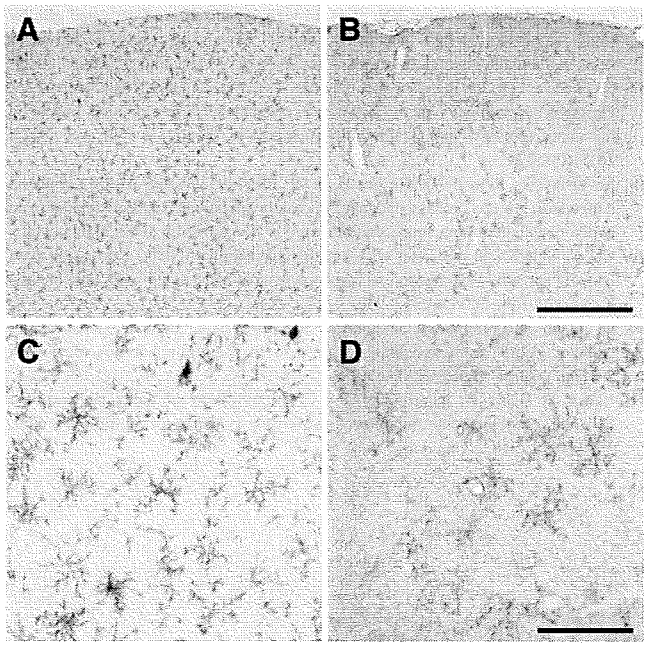

FIGURE 7. Photomicrographs of OX-42 immunoreactivity after cortical spreading depression. Images display OX-42 immunoreactivity 8 d after 2 h of recurrent spreading depression in left hemisphere (A and C), compared with contralateral hemisphere (B and D). (C and D) Magnified views of OX-42 immunoreactivity. Hypertrophied or ameboid OX-42–positive microglial cells were often seen in left hemisphere. Bars in B and D indicate 500 and 100 μm, respectively.

observations suggest that ^{11}C-PK11195 PET is potentially useful for the quantitative evaluation of temporal change in neurogenic inflammation in the rat model of migraine.

CONCLUSION

In the present study, we evaluated for the first time, to our knowledge, the neurogenic inflammation in the rat model of migraine using quantitative PET with ^{11}C-PK11195. The microglial activation quantified by ^{11}C-PK11195 PET was significantly increased in the cerebral hemisphere, which underwent unilateral cortical spreading depression. These results suggest that ^{11}C-PK11195 PET is useful for the evaluation of the neurogenic inflammatory process and may provide a new and powerful tool for both the diagnosis of migraine and the monitoring efficacy for migraine therapy.

ACKNOWLEDGMENT

This work was supported in part by a consignment expense from the Molecular Imaging Program on "Research Base for Exploring New Drugs" from the Ministry of Education, Culture, Sports, Science, and Technology (MEXT), Japanese government.

REFERENCES

1. Kreutzberg GW. Microglia: a sensor for pathological events in the CNS. *Trends Neurosci.* 1996;19:312–318.
2. Streit WJ, Mrak RE, Griffin WS. Microglia and neuroinflammation: a pathological perspective. *J Neuroinflammation.* 2004;1:14.
3. Dalessio DJ. A classification of headache. *Int Ophthalmol Clin.* 1970;10: 647–665.
4. Markowitz S, Saito K, Moskowitz MA. Neurogenically mediated leakage of plasma protein occurs from blood vessels in dura mater but not brain. *J Neurosci.* 1987;7:4129–4136.
5. Moskowitz MA. The neurobiology of vascular head pain. *Ann Neurol.* 1984;16:157–168.
6. Arnold G, Reuter U, Kinze S, Wolf T, Einhaupl KM. Migraine with aura shows gadolinium enhancement which is reversed following prophylactic treatment. *Cephalalgia.* 1998;18:644–646.
7. Iizuka T, Sakai F, Suzuki K, Igarashi H, Suzuki N. Implication of augmented vasogenic leakage in the mechanism of persistent aura in sporadic hemiplegic migraine. *Cephalalgia.* 2006;26:332–335.
8. Goadsby PJ, Edvinsson L, Ekman R. Vasoactive peptide release in the extracerebral circulation of humans during migraine headache. *Ann Neurol.* 1990;28:183–187.
9. Peroutka SJ. Neurogenic inflammation and migraine: implications for the therapeutics. *Mol Interv.* 2005;5:304–311.
10. Moran LB, Duke DC, Turkheimer FE, Banati RB, Graeber MB. Towards a transcriptome definition of microglial cells. *Neurogenetics.* 2004;5:95–108.
11. Benavides J, Guilloux F, Rufat P, et al. In vivo labelling in several rat tissues of 'peripheral type' benzodiazepine binding sites. *Eur J Pharmacol.* 1984;99:1–7.
12. Cagnin A, Gerhard A, Banati RB. In vivo imaging of neuroinflammation. *Eur Neuropsychopharmacol.* 2002;12:581–586.
13. Casellas P, Galiegue S, Basile AS. Peripheral benzodiazepine receptors and mitochondrial function. *Neurochem Int.* 2002;40:475–486.
14. Price CJ, Wang D, Menon DK, et al. Intrinsic activated microglia map to the peri-infarct zone in the subacute phase of ischemic stroke. *Stroke.* 2006;37: 1749–1753.
15. Banati RB, Newcombe J, Gunn RN, et al. The peripheral benzodiazepine binding site in the brain in multiple sclerosis: quantitative in vivo imaging of microglia as a measure of disease activity. *Brain.* 2000;123:2321–2337.
16. Cagnin A, Brooks DJ, Kennedy AM, et al. In-vivo measurement of activated microglia in dementia. *Lancet.* 2001;358:461–467.
17. Gerhard A, Pavese N, Hotton G, et al. In vivo imaging of microglial activation with [^{11}C](*R*)-PK11195 PET in idiopathic Parkinson's disease. *Neurobiol Dis.* 2006;21:404–412.
18. Pavese N, Gerhard A, Tai YF, et al. Microglial activation correlates with severity in Huntington disease: a clinical and PET study. *Neurology.* 2006;66: 1638–1643.
19. Leao AAP. Spreading depression of activity in the cerebral cortex. *J Neurophysiol.* 1944;7:359–390.
20. Nedergaard M, Hansen AJ. Spreading depression is not associated with neuronal injury in the normal brain. *Brain Res.* 1988;449:395–398.
21. Cui Y, Kataoka Y, Li QH, et al. Targeted tissue oxidation in the cerebral cortex induces local prolonged depolarization and cortical spreading depression in the rat brain. *Biochem Biophys Res Commun.* 2003;300:631–636.
22. Milner PM. Note on a possible correspondence between the scotomas of migraine and spreading depression of Leao. *Electroencephalogr Clin Neurophysiol.* 1958;10:705.
23. Lauritzen M, Skyhoj Olsen T, Lassen NA, Paulson OB. Changes in regional cerebral blood flow during the course of classic migraine attacks. *Ann Neurol.* 1983;13:633–641.
24. Olesen J, Larsen B, Lauritzen M. Focal hyperemia followed by spreading oligemia and impaired activation of rCBF in classic migraine. *Ann Neurol.* 1981;9:344–352.
25. Hadjikhani N, Sanchez Del Rio M, Wu O, et al. Mechanisms of migraine aura revealed by functional MRI in human visual cortex. *Proc Natl Acad Sci USA.* 2001;98:4687–4692.
26. Eikermann-Haerter K, Moskowitz MA. Animal models of migraine headache and aura. *Curr Opin Neurol.* 2008;21:294–300.
27. Lauritzen M. Pathophysiology of the migraine aura: the spreading depression theory. *Brain.* 1994;117:199–210.
28. *Guide for the Care and Use of Laboratory Animals.* Washington, DC: Government Printing Office; 1985. NIH publication 85-23.
29. Shah F, Hume SP, Pike VW, Ashworth S, McDermott J. Synthesis of the enantiomers of [*N*-methyl-^{11}C]PK 11195 and comparison of their behaviours as radioligands for PK binding sites in rats. *Nucl Med Biol.* 1994;21:573–581.

30. Schweinhardt P, Fransson P, Olson L, Spenger C, Andersson JL. A template for spatial normalisation of MR images of the rat brain. *J Neurosci Methods.* 2003;129:105–113.
31. Logan J, Fowler JS, Volkow ND, Wang GJ, Ding YS, Alexoff DL. Distribution volume ratios without blood sampling from graphical analysis of PET data. *J Cereb Blood Flow Metab.* 1996;16:834–840.
32. Back T, Kohno K, Hossmann KA. Cortical negative DC deflections following middle cerebral artery occlusion and KCl-induced spreading depression: effect on blood flow, tissue oxygenation, and electroencephalogram. *J Cereb Blood Flow Metab.* 1994;14:12–19.
33. Boutin H, Chauveau F, Thominiaux C, et al. ^{11}C-DPA-713: a novel peripheral benzodiazepine receptor PET ligand for in vivo imaging of neuroinflammation. *J Nucl Med.* 2007;48:573–581.
34. Gulyas B, Halldin C, Vas A, et al. [^{11}C]vinpocetine: a prospective peripheral benzodiazepine receptor ligand for primate PET studies. *J Neurol Sci.* 2005; 229–230:219–223.
35. Banati RB, Goerres GW, Myers R, et al. [^{11}C](*R*)-PK11195 positron emission tomography imaging of activated microglia in vivo in Rasmussen's encephalitis. *Neurology.* 1999;53:2199–2203.
36. Cagnin A, Myers R, Gunn RN, et al. In vivo visualization of activated glia by [^{11}C] (*R*)-PK11195-PET following herpes encephalitis reveals projected neuronal damage beyond the primary focal lesion. *Brain.* 2001;124:2014–2027.
37. Stephenson DT, Schober DA, Smalstig EB, Mincy RE, Gehlert DR, Clemens JA. Peripheral benzodiazepine receptors are colocalized with activated microglia following transient global forebrain ischemia in the rat. *J Neurosci.* 1995; 15:5263–5274.
38. Vowinckel E, Reutens D, Becher B, et al. PK11195 binding to the peripheral benzodiazepine receptor as a marker of microglia activation in multiple sclerosis and experimental autoimmune encephalomyelitis. *J Neurosci Res.* 1997;50:345–353.
39. Cui Y, Kataoka Y, Inui T, et al. Up-regulated neuronal COX-2 expression after cortical spreading depression is involved in non-REM sleep induction in rats. *J Neurosci Res.* 2008;86:929–936.
40. Caggiano AO, Kraig RP. Eicosanoids and nitric oxide influence induction of reactive gliosis from spreading depression in microglia but not astrocytes. *J Comp Neurol.* 1996;369:93–108.
41. Itzhak Y, Baker L, Norenberg MD. Characterization of the peripheral-type benzodiazepine receptors in cultured astrocytes: evidence for multiplicity. *Glia.* 1993;9:211–218.

High Energy Resolution Hard X-Ray and Gamma-Ray Imagers Using CdTe Diode Devices

Shin Watanabe, Shin-nosuke Ishikawa, Hiroyuki Aono, Shin'ichiro Takeda, Hirokazu Odaka, Motohide Kokubun, Tadayuki Takahashi, Kazuhiro Nakazawa, Hiroyasu Tajima, Mitsunobu Onishi, and Yoshikatsu Kuroda

Abstract—**We developed CdTe double-sided strip detectors (DSDs or cross strip detectors) and evaluated their spectral and imaging performance for hard X-rays and gamma-rays. Though the double-sided strip configuration is suitable for imagers with a fine position resolution and a large detection area, CdTe diode DSDs with indium (In) anodes have yet to be realized due to the difficulty posed by the segmented In anodes. CdTe diode devices with aluminum (Al) anodes were recently established, followed by a CdTe device in which the Al anodes could be segmented into strips. We developed CdTe double-sided strip devices having Pt cathode strips and Al anode strips, and assembled prototype CdTe DSDs. These prototypes have a strip pitch of 400 μm. Signals from the strips are processed with analog ASICs (application specific integrated circuits). We have successfully performed gamma-ray imaging spectroscopy with a position resolution of 400 μm. Energy resolution of 1.8 keV (FWHM: full width at half maximum) was obtained at 59.54 keV. Moreover, the possibility of improved spectral performance by utilizing the energy information of both side strips was demonstrated. We designed and fabricated a new analog ASIC, VA32TA6, for the readout of semiconductor detectors, which is also suitable for DSDs. A new feature of the ASIC is its internal ADC function. We confirmed this function and good noise performance that reaches an equivalent noise charge of 110 e^- under the condition of 3–4 pF input capacitance.**

Index Terms—**CdTe detectors, CZT detectors, gamma-ray detectors, imaging Spectrometers, strip detectors.**

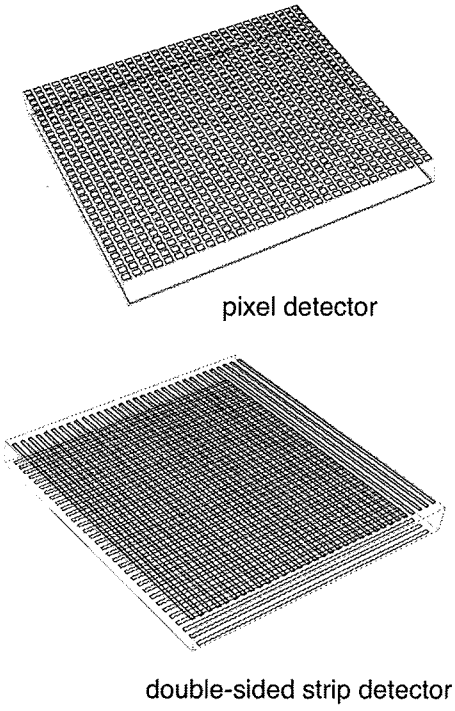

Fig. 1. Pixel detector and double-sided strip detector.

I. Introduction

HARD X-ray and gamma-ray imaging spectrometers with good spatial and energy resolutions are desired for medical, industrial and astrophysical applications. Cadmium telluride (CdTe) and cadmium zinc telluride (CZT) are very promising materials for hard X-ray and gamma-ray imaging spectrometers, given their high detection efficiency comparable to that of NaI scintillators and good energy resolution comparable to that of Ge detectors. Although both CdTe and CZT are vulnerable to energy resolution and peak detection efficiency being degraded due to their poor charge transport properties, several techniques have been developed to maintain good spectral performance [1], [2].

CdTe/CZT semiconductor detectors require segmented readout electrodes in order to obtain position information. For imagers having a fine position resolution, there are two types of detector configurations: pixel detectors and double-sided strip detectors (Fig. 1).

A pixel detector has a number of small pixel electrodes on one side. The signal from each pixel is processed with each charge-sensitive amplifier. Since the leakage current and the detector capacitance become very small, ideal spectral performance is consequently possible. However, an extremely large number of readout channels are needed for a fine position resolution and/or large detection area. Additionally, a two-dimensional readout ASIC is essential for fine pitch pixels [3]–[5].

Manuscript received June 30, 2008; revised September 12, 2008. Current version published June 17, 2009. This work was supported by KAKENHI(19740172).

S. Watanabe, S. Ishikawa, H. Aono, S. Takeda, H. Odaka, and T. Takahashi are with the Institute of Space and Astronautical Science, Japan Aerospace Exploration Agency, Sagamihara, Kanagawa, Japan, and also with the Department of Physics, University of Tokyo, Tokyo, Japan (e-mail: watanabe@astro.isas.jaxa.jp; ishikawa@astro.isas.jaxa.jp; aono@astro.isas.jaxa.jp; takeda@astro.isas.jaxa.jp; odaka@astro.isas.jaxa.jp; takahasi@astro.isas.jaxa.jp).

M. Kokubun is with the Institute of Space and Astronautical Science, Japan Aerospace Exploration Agency, Sagamihara, Kanagawa, Japan (e-mail: kokubun@astro.isas.jaxa.jp).

K. Nakazawa is with the Department of Physics, University of Tokyo, Tokyo, Japan (e-mail: nakazawa@amalthea.phys.s.u-tokyo.ac.jp).

H. Tajima is with the SLAC National Accelerator Laboratory, Menlo Park, CA 94025 USA (e-mail: htajima@slac.stanford.edu).

M. Onishi and Y. Kuroda are with Nagoya Guidance and Propulsion Systems Works, Mitsubishi Heavy Industry. Ltd., Komaki, Aichi, Japan (e-mail: mitsunobu_onishi@mhi.co.jp; yoshikatsu_kuroda@mhi.co.jp).

Digital Object Identifier 10.1109/TNS.2008.2008806

A double-sided strip detector (DSD or cross strip detector) realizes a fine position resolution and large detection area with a relatively small number of readout channels. The DSD has orthogonal strips implemented on both its sides. By reading out the signal from both side strips coincidentally, it is possible to obtain information on the position and energy of the X-ray/gamma-ray photons [6], [7]. The number of the readout channels is proportional to $2N$ (where N denotes the number of segments per coordinate) for DSDs, instead of N^2 for pixel detectors. Therefore, for a larger N (meaning a finer position resolution and/or larger area), the DSD has an advantage in terms of readout channels. Moreover, one-dimensional ASICs that are easier to implement and more common than two-dimensional ones are also applicable to DSDs.

Our development is aimed at hard X-ray imaging detectors for the ASTRO-H (NeXT) project that plans to launch Japan's 6th X-ray astronomy satellite in 2013. Among the major objectives is achieving high sensitivity observation with focusing and imaging capabilities in the 5–80 keV energy region. The ASTRO-H satellite will carry two hard X-ray telescopes that feature multilayer supermirrors assembled in grazing incident X-ray telescopes. Hard X-ray Imagers (the focal plane detectors of hard X-ray telescopes) require an energy resolution of $\sim$1 keV (FWHM: full width at half maximum), energy coverage of 5–80 keV, a sub-mm (250–500 μm) position resolution, detection area of 2–3 cm, and timing resolution of $\sim$ 1 μs for high sensitivity observation. To achieve these goals, we have developed CdTe diode DSDs as a primary choice for Hard X-ray Imagers. In this paper, we describe our development of CdTe DSDs, and report the results of the CdTe DSD prototypes. We also report on our newly developed ASIC (VA32TA6) for semiconductor detector readout.

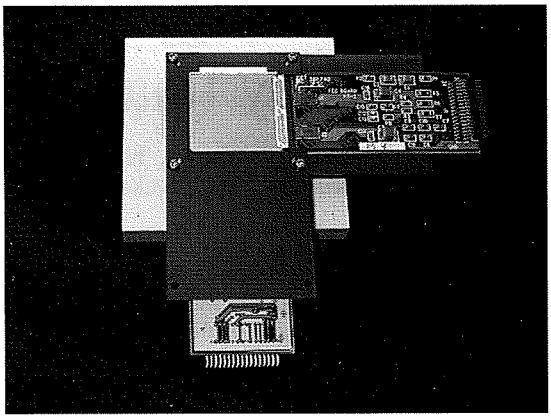

(a)

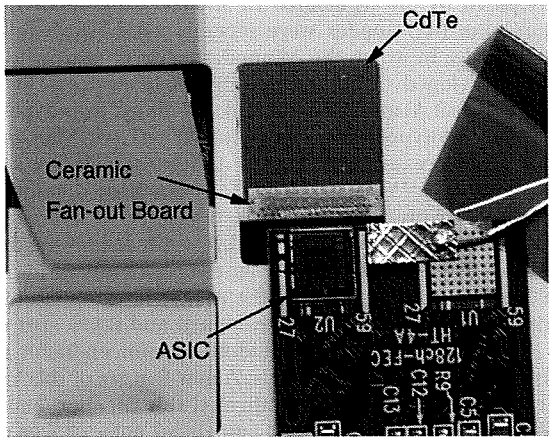

(b)

Fig. 2. Prototypes of the CdTe DSDs. (a): The 2.6 cm CdTe DSD. It is 2.6 cm $\times$ 2.6 cm in size and, 500 μm thick. The strip pitch is 400 μm. On each side 64 strips are formed, and two VA32TAs are used for readout on each side. (b): The 1.3 cm CdTe DSD. It is 1.3 cm $\times$ 1.3 cm in size, and 500 μm thick. The strip pitch is 400 μm. On each side 32 strips are formed, and one VA64TA2 is used for readout on each side.

II. Prototypes of CdTe DSDs

A. CdTe Diode Device With Double-Sided Strips

Thin CdTe diode devices that utilize indium (In) as the anode electrodes on p-type CdTe wafers manufactured by ACRORAD (Japan) and platinum (Pt) as the cathodes have been established and offer good spectral performance [1]. A high Schottky barrier formed on the In/p-CdTe interface enables use of the detector as a diode. Using this type of detector with a thickness of 0.5 mm at applied bias voltages as high as 1 kV makes it possible to overcome the poor charge transport properties of CdTe. However, double-sided strip detectors with In anodes cannot be realized since it is difficult to segment the In electrode into strips.

Aluminum (Al) has recently been found to be a good alternative electrode material to In [8], [9]. In addition to low leakage currents and high energy resolutions comparable to those of In/CdTe/Pt detectors, Al/CdTe/Pt detectors also offer the advantage of allowing Al anodes to be divided into pixels or strips. CdTe diode detectors with segmented Al anodes have been established by constructing and testing Al-pad/CdTe/Pt or Al-pixel/CdTe/Pt type detectors. Good spectral performance ($\Delta E \sim$ 1 keV (FWHM) at 60 keV) has been achieved [10], [11].

By adopting segmented Al anodes and Pt cathodes, we can obtain a CdTe diode double-sided strip device. For the prototype detectors, we fabricated two types of the CdTe devices: the 2.6 cm CdTe device and 1.3 cm CdTe device. The 2.6 cm CdTe device is 2.6 cm $\times$ 2.6 cm in size, and 500 μm thick. On each side 64 strips are formed, with a strip pitch of 400 μm. Moreover, 350 μm strip electrodes and 50 μm gaps are alternately formed. The 1.3 cm CdTe device is 1.3 cm $\times$ 1.3 cm in size, and 500 μm thick. On each side 32 strips are formed. The strip pitch and electrode configuration are the same as those of the 2.6 cm CdTe DSD. Both devices have guard-ring electrodes on both sides to reduce leakage current of the strips.

B. Configurations of Prototypes

We used the CdTe double-sided strip devices described above to assemble two types of prototype CdTe DSDs: the 2.6 cm CdTe DSD and the 1.3 cm CdTe DSD. Fig. 2 shows the prototype detectors. We employed VA32TAs [12] and VA64TA2s [13] that we jointly developed with GM-IDEAS to read out the 2.6 cm and the 1.3 cm CdTe DSDs, respectively.

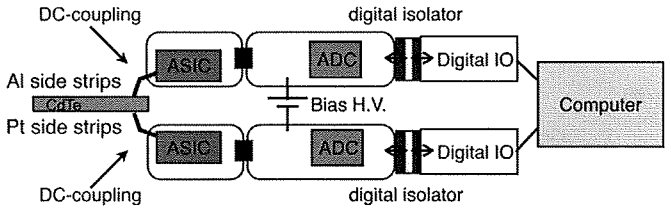

Fig. 3. Readout system of the CdTe DSDs.

Given the soft and fragile characteristics of CdTe material, we have yet to establish a reliable technique of wire-bonding on the CdTe surface. Therefore, it is difficult to interconnect the CdTe strip electrodes and the readout ASIC input pads by using wire-bonding as applied to Si DSDs [14], [15].

To overcome this problem, we adopted the In/Au stud bump bonding technique and used the Al_2O_3 ceramic fan-out board with through-holes. First, the CdTe strip electrodes are connected via In/Au stud bump bonding to the Al_2O_3 ceramic fan-out board that we developed and established for CdTe-Pixel/Pad detectors [16]. This ceramic fan-out board has through-holes to interconnect the electrodes on both sides of the fan-out board. Then, wire-bonding can be done from the ASIC input pads to the electrodes on the ceramic board. We have connected readout ASICs on both sides of the CdTe DSDs in this manner. A more detailed procedure is described in elsewhere [17].

Fig. 3 shows a block diagram illustrating the overall readout system. This system is virtually the same as the scheme implemented for the readout of Si DSDs [14], [15]. The readout ASICs and strip electrodes are connected with DC-coupling for both sides. The detector bias voltage is supplied by applying a high voltage between local grounds of the Al anodes and Pt cathodes.

C. Imaging and Spectral Performance

In order to demonstrate the imaging capability of the test devices, we took shadow images of metal objects with various gamma rays from radioisotopes such as ^{241}Am, ^{133}Ba and ^{57}Co. Fig. 4 shows the shadow images obtained with the 2.6 cm CdTe DSD and the target. The hole of a 2-mm nut and solder 0.6 mm diameter can be clearly seen. It can also be seen that a thin washer becomes transparent as the energy of gamma rays becomes higher. However, the energy resolution obtained with the 2.6 cm CdTe DSD did not match that obtained with pad-type Al anode detectors. FWHM energy resolutions of 2.6 keV and 6.2 keV at 59.54 keV were obtained for the spectra from Pt strips and Al strips, respectively, under 500 V of bias voltage and temperature of $-20°$C.

For a detailed study of spectral performance, we tested a 1.3 cm CdTe DSD. The smaller capacitance and lower leakage current afforded by smaller detector size should lead us to better noise performance. The spectral performance of VA64TA2 for negative signals from the Al strips has also been improved compared with VA32TA used in the 2.6 cm CdTe DSD.

Fig. 5 show the spectra obtained with the 1.3 cm CdTe DSD. Under operating conditions of $-20°$C temperature and 500 V of applied bias voltage, the total leakage current from all strips and guard-rings was 5 nA. The trigger energy threshold can be set to about 10 keV. An energy resolution of 1.8 keV (FWHM) at 59.54 keV was obtained for both the Pt and Al sides. The spectral performance for the Al and Pt sides was confirmed as being equivalent in the CdTe DSDs.

By collectively using the energy information on both sides, improved spectral performance could be expected if each noise component was independent. We created a spectrum by filling the average of the both sides' energy information, as shown in Fig. 6. This spectrum shows improved energy resolution. Thus, an energy resolution of 1.4 keV (FWHM) was successfully obtained.

For imagers, uniform spectral performance in each detector is important. In the double-sided strip configuration, we can examine a kind of uniformity by sorting the events of one strip based on the position information obtained from the other side's strips. Since only one channel of the ASIC is used for the readout, we can obtain the position dependence without the effect of readout variation. Fig. 7 shows a ^{241}Am gamma-ray spectrum from one strip on the Al side. The Y axis corresponds to the hit strip on the Pt side. It can be seen that the spectrum is constant with the position. The peak position and energy resolution for 59.54 keV gamma rays were stable within 0.2% and 12%, respectively.

III. Brand New Readout ASIC, VA32TA6

We have been developing readout ASICs for our applications in collaboration with GM-IDEAS. Based on past developments, we designed and fabricated a new readout ASIC, VA32TA6. Fig. 8 shows a photograph of VA32TA6 and a schematic diagram of the ASIC. VA32TA6 is fabricated using AMS 0.35 μm technology with an epitaxial layer. The die is 5.0 mm $\times$ 7.8 mm in size and 725 μm thick. The front-end part of VA32TA6 is based on VA64TA1 [13]. It has 32 channels of circuits, including a charge-sensitive amplifier, slow CR-RC shaper and sample/hold (VA section), and fast CR-RC shaper and discriminator chain (TA section). The shaping time of the slow shaper is variable from 2 to 4 μs: that of the fast shaper is 600 ns. A detailed description of this VA-TA architecture is given in other [12], [14]. The measured power consumption on average was 16.5 mW per chip, corresponding to 0.5 mW per channel by considering a simple division of channel numbers.

The main new feature of VA32TA6 is the inclusion of on-chip ADC circuitry. VA32TA6 implements a Wilkinson-type ADC that digitizes the 32 sampled pulse heights of the slow shapers in parallel. The ramp speed is adjustable via the internal DAC. The ADC clock's maximum speed is 10 MHz. Each channel has a 10-bit digital counter. The maximum dead time due to AD conversion is $\sim$ 100 μs under the 10 MHz ADC clock. The ADC circuitry is equipped with a global Common Mode Detection Unit. This unit latches the ADC counter value when a certain number of channel discriminators have fired. For VA32TA6, the threshold of the Common Mode Detection Unit has one default setting (16 channels). The common mode value is stored in a separate counter and output as part of the data stream.

To evaluate the functions and performance of the ASIC, we constructed CdTe pad detectors for connection to VA32TA6. Each pad is 1.35 mm $\times$ 1.35 mm in size. A total of 32 pads

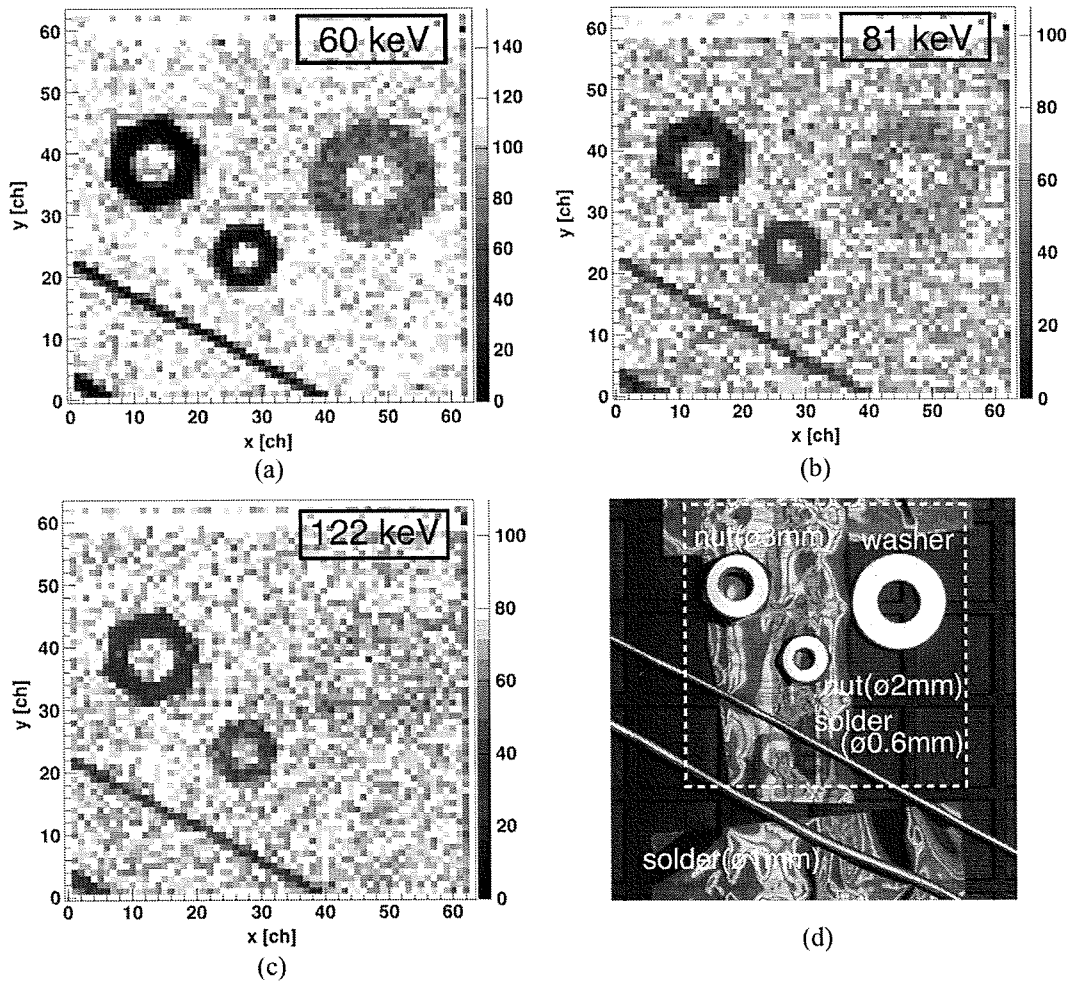

Fig. 4. Shadow images obtained with the 2.6 cm CdTe DSD and a photograph of the target. The energies of the gamma rays are 60 keV (^{241}Am), 81 keV (^{133}Ba) and 122 keV (^{57}Co). The pixel size in the images corresponds to a strip pitch of 400 μm.

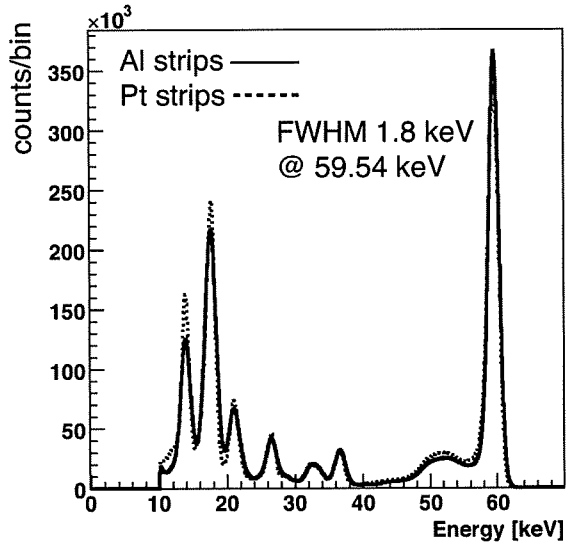

Fig. 5. ^{241}Am spectra obtained with the 1.3 cm CdTe DSD. The solid and dotted lines indicate spectra from the Al and Pt strips, respectively. A bias voltage of 500 V was applied at operating temperature of −20°C. An energy resolution of 1.8 keV(FWHM) at 59.54 keV was obtained for both sides.

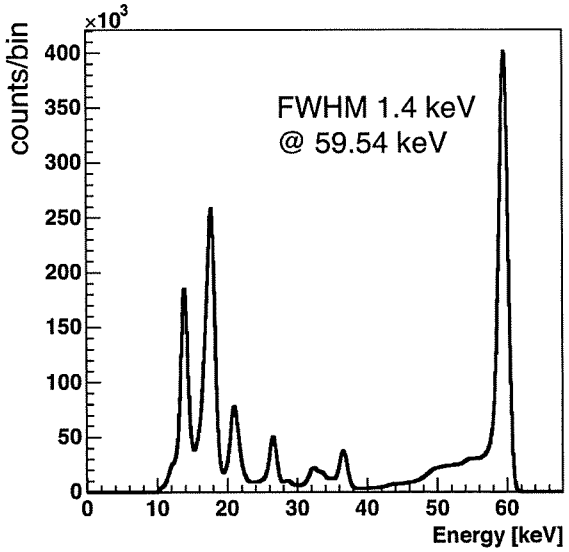

Fig. 6. ^{241}Am spectra obtained with the 1.3 cm CdTe DSD. The average of the both sides' energy information was used. The energy resolution was improved to 1.4 keV(FWHM) at 59.54 keV.

(in 8 × 8 = 64 pads) are connected to the ASIC. The pad capacitance is expected to be 3–4 pF per channel. We used two types of CdTe pad detectors. One is an In/CdTe/Pt-pad type detector [18], in which VA32TA6 is connected to Pt cathode pads, for processing positive charge signals. The other is an

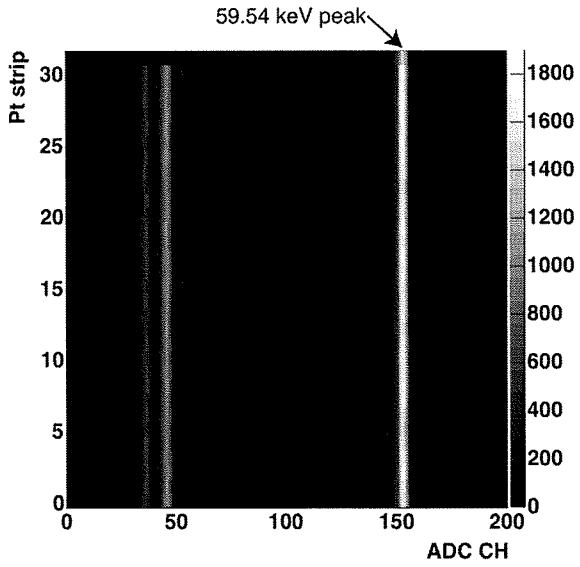

Fig. 7. ^{241}Am spectra obtained with one Al strip of the 1.3 cm CdTe DSD. The X and Y axes correspond to the Al strip's pulse height in the ADC channel and the hit strip on the Pt side, respectively.

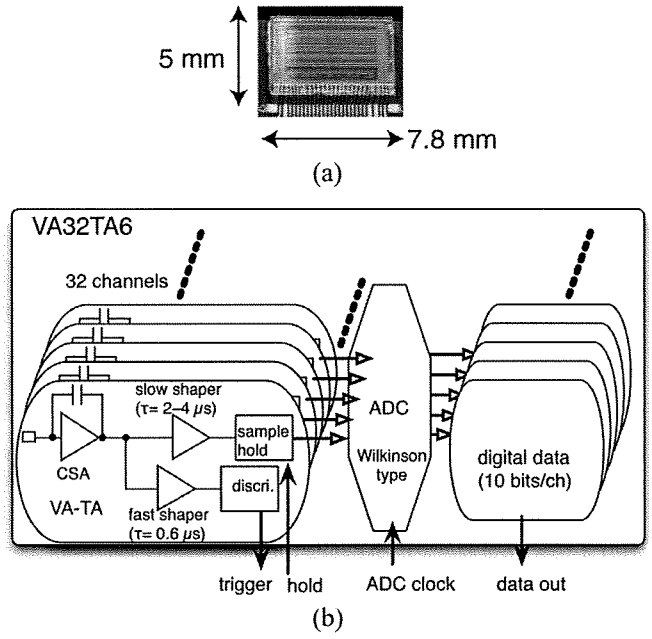

Fig. 8. Photograph of VA32TA6 and a schematic diagram.

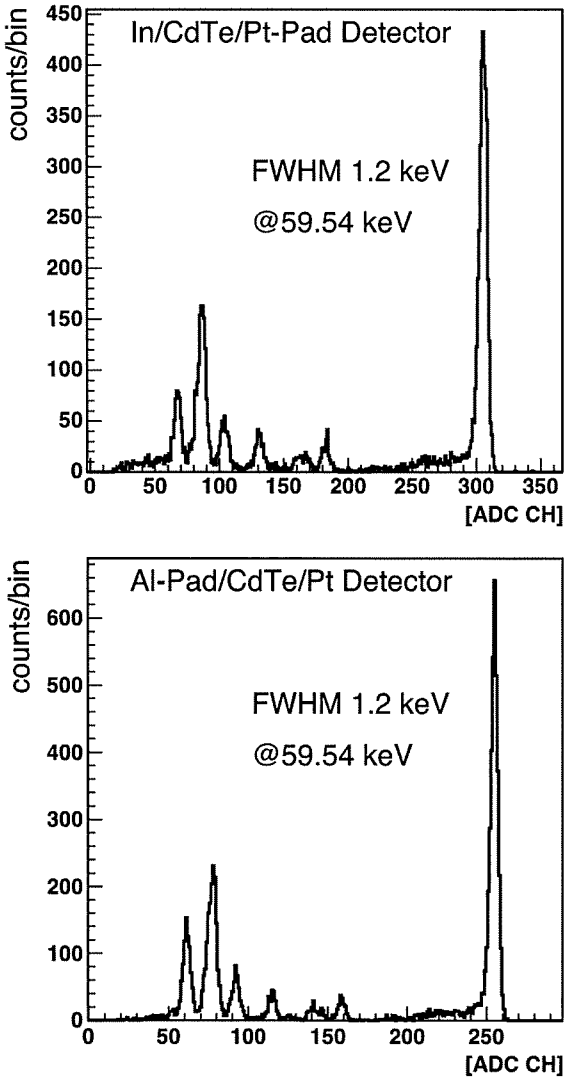

Fig. 9. ^{241}Am gamma-ray spectra obtained with CdTe pad detectors using VA32TA6. At an operating temperature of −20°C, bias voltages of 600 V and 400 V were applied for the In/CdTe/Pt-pad detector and Al-pad/CdTe/Pt detector, respectively. The pedestal level was corrected, and the common mode was subtracted by using the data from the Common Mode Detection Unit. An energy resolution of 1.2 keV (FWHM) at 59.54 keV was achieved.

Al-pad/CdTe/Pt type detector [10]. The ASIC in this detector is connected to Al anode pads for processing negative charge signals.

By applying a detector bias voltage and irradiating the detector with X-rays/gamma rays emitted by a radioisotope, we have successfully made VA32TA6s work and have obtained digital pulse height data. The ADC circuitry works properly with clock speed up to 10 MHz. Fig. 9 shows the obtained spectra from the CdTe pad detectors. These spectra are obtained from a single channel of the pad detectors. The pedestal level is corrected, and the common mode is subtracted by using the data from the Common Mode Detection Unit. An energy resolution of 1.2 keV (FWHM) at 59.54 keV was achieved for both pad detectors. This energy resolution in CdTe corresponds to 110 e^- in ENC (equivalent noise charge). This spectral performance is comparable with that of VA64TA1 [13].

For our astrophysical application, it is important to achieve as low an energy threshold as possible. Fig. 10 demonstrates the low energy threshold. This is an X-ray spectrum from ^{55}Fe obtained with one channel of the Al-pad/CdTe/Pt detector. The Mn K X-ray line combining a 5.9 keV Kα and a 6.4 keV Kβ was detected and clearly resolved. The energy threshold can be set as low as 4 keV, which satisfies the energy coverage goal of Hard X-ray Imagers used in the ASTRO-H (NeXT) project.

IV. Conclusion

We developed CdTe diode double-sided strip detectors that have Al anode and Pt cathode strips. Two types of prototypes were assembled and we evaluated their imaging capability and